The Astrophysical Journal Letters, 873:L11 (9pp), 2019 March 10 https://doi.org/10.3847/2041-8213/ab07bd

Mega-Gauss Plasma Jet Creation Using a Ring of Laser Beams

L. Gao[1], E. Liang[2], Y. Lu[2,3], R. K. Follet[4], H. Sio[5], P. Tzeferacos[6], D. H. Froula[4], A. Birkel[5], C. K. Li[5], D. Lamb[6], R. Petrasso[5], W. Fu[2], M. Wei[7], and H. Ji[1]

[1] Princeton Plasma Physics Laboratory, Princeton University, Princeton, NJ 08536, USA
[2] Rice University, Houston, TX 77005, USA; liang@rice.edu
[3] Los Alamos National Laboratory, Los Alamos, NM 87545, USA
[4] Laboratory for Laser Energetics, Rochester, NY 14623, USA
[5] Plasma Science and Fusion Center, Massachusetts Institute of Technology, Cambridge, MA 02139, USA
[6] Department of Astronomy and Astrophysics, University of Chicago, Chicago, IL 60637, USA
[7] Laboratory for Laser Energetics, University of Rochester, Rochester, NY 14623, USA
Received 2019 January 13; revised 2019 February 12; accepted 2019 February 13; published 2019 March 8

Abstract

Using 20 OMEGA laser beams at the Laboratory for Laser Energetics, University of Rochester, to irradiate a flat plastic target in a hollow ring configuration, we created supersonic cylindrical stable plasma jets with self-generated megagauss magnetic fields extending out to >4 mm. These well-collimated magnetized jets possess a number of distinct and novel properties that will allow us to study the dynamics, physical processes, and scaling properties of astrophysical jets with a dynamic range exceeding those of previous laboratory settings. The dimensionless parameters of these laboratory jets fall in the same regime as those of young stellar object jets. These jets will also provide new versatile laser-based platforms to study magnetized shocks, shear flows, and other plasma processes under controllable conditions.

Key words: hydrodynamics – magnetic fields – stars: jets

1. Introduction

Magnetized plasma jets are ubiquitous in the universe (Ferrari 1998; Livio 1999; Sari et al. 1999; Bally et al. 2007; Frank et al. 2014). It is thus highly desirable to recreate them in the laboratory to study their physical processes and scaling properties under controllable conditions. Recently, the irradiation of solid targets with high-energy lasers has become a popular tool to launch supersonic plasma outflows for a broad range of applications, including the study of astrophysical jets (see articles in Hartigan 2013; Ciardi 2015).

When an intense laser irradiates a solid target, strong toroidal magnetic fields are created around the laser spot by the $\nabla P_e \times \nabla n_e$ term ("Biermann battery," where P_e = electron pressure, n_e = electron density, Biermann 1950) of the generalized Ohm's law (Krall & Trivelpiece 1973; Epperlein 1984; Epperlein & Haines 1986). However, these magnetic fields are localized at the surface, spanning distances $\leqslant$ a few times laser spot size. They decay rapidly in time and space as the outflow expands, diverges, and rarifies. Hence the creation of stable cylindrical plasma jets with strong self-generated magnetic fields at large distances from the laser target remains an unsolved challenge. Here we report a new laser platform capable of creating stable cylindrical plasma jets with megagauss (MG) self-generated fields extending to >4 mm, by using 20 OMEGA laser beams with 10 kJ total energy at the Laboratory for Laser Energetics (LLE; Boehly et al. 1995) of the University of Rochester, to irradiate a flat CH target in a hollow ring pattern. We use CH as the baseline target material because its radiative cooling effect is small and dynamically unimportant. For comparison we also added high-*Z* dopant to the CH target to study the effects of radiative cooling on jet properties (see Section 3).

The goal of our laser experiment is to create hydrodynamic collimated jets with the strongest self-generated magnetic fields extending to the largest distance from target. Hence it is useful to first review some of the previous laboratory jet experiments. Large-scale magnetized jets had been previously created using pulse power machines by many groups (Lebedev et al. 2002, 2005; Gourdain et al. 2010; Suzuki-Vidal et al. 2011). These jets mostly consist of low-density plasmas ($n_e \leqslant 10^{19}\mathrm{cm}^{-3}$) accelerated by externally induced $\boldsymbol{j}\mathrm{x}\boldsymbol{B}$ forces ($\boldsymbol{j}$ = current, $\boldsymbol{B}$ = magnetic field) and collimated by strong toroidal fields. Therefore, their dynamics and physical properties are fundamentally different from those of hydrodynamic jets launched by laser-solid-target interactions.

Beginning in the 1990s, laser-driven hydrodynamic jets have been created by irradiating cone-shaped or V-shaped foil targets to thermalize the transverse momentum and facilitate axial collimation of the outflow (Farley et al. 1999; Gregory et al. 2008). A series of experiments to study radiative jet formation and interaction with ambient material was conducted by the group at the Prague Asterix Laser System (PALS), by varying the focal spot size of a single laser beam irradiating different flat metal targets (Kasperczuk et al. 2006; Nicolaï et al. 2006, 2008; Pisarczyk et al. 2007; Tikhonchuk et al. 2008). In all these early laser-driven hydrodynamic jet experiments, collimation were achieved by radiative cooling and radial collapse, and no magnetic field measurements were made. Though the laser intensity profile of the PALS experiments became concave and ring-like as the focal spot radius was increased, these authors firmly established that the primary factor in their jet collimation was radiative cooling and radial collapse (Kasperczuk et al. 2006; Nicolaï et al. 2006). Detailed numerical simulations of the PALS experiments also found that no significant magnetic field was created far from the target (Nicolaï et al. 2006). This is expected as the electron pressure and density gradients interior to the single laser spot are insufficient to create strong Biermann-battery fields far away from the target surface. FLASH simulations clearly show that to create strong Biermann-battery fields far from the laser target, one needs a hollow ring radius $\ll$ the width of the ring, which was not the case in the PALS experiments, where the laser spot size and annular width were comparable.

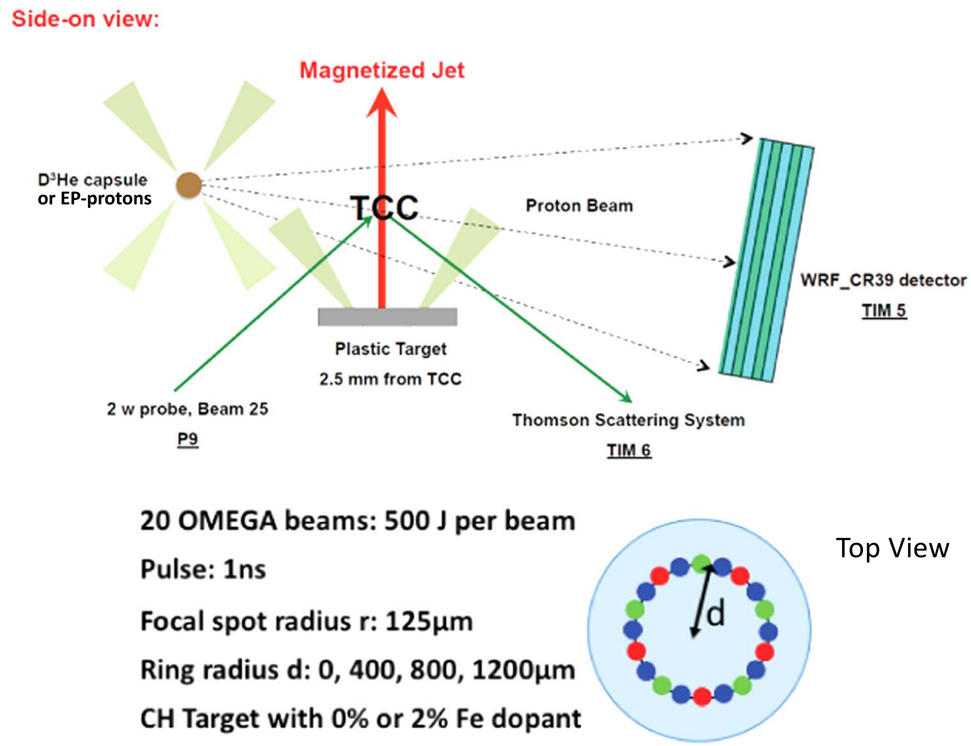

Figure 1. Setup of the OMEGA magnetized jet experiment. Laser parameters and top view of 20-beam pattern (colors denote different incident angles) are illustrated in the lower figure. The CH target is located 2.5 mm below target chamber center (TCC). D^3He or OMEGA-EP proton sources are located ~1 cm to the left of TCC and proton images are recorded at 16.5–17 cm to the right of TCC. A $2\omega_o$ TS probe beam measured plasma parameters at TCC with ~50 μm spatial resolution. Not shown is the XRFC, which looks down at ~38° from the jet axis.

More recently, a strongly magnetized jet-like outflow was created using two OMEGA laser beams to irradiate a V-shaped foil, such that the collision of the two blow-offs leads to the reconnection and advection of their combined Biermann-battery fields (Li et al. 2016). However, this setup was inherently non-cylindrical and the jet was unstable due to magnetohydrodynamic (MHD) and geometric effects. While this experiment was relevant to studying the kinks of the Crab pulsar jet, most long narrow astrophysical jets appear to be stable. Consequently, the dynamics and long-range stability of cylindrical jets cannot be faithfully studied using the V-foil collision platform. The magnetized jets created using a hollow ring of laser beams irradiating flat targets reported here are inherently cylindrical and stable to first order, and exhibit well-defined scaling properties with the ring radius. As we will discuss below, hollow-ring-laser-driven jets have many special and desirable properties not found in jets created using these other schemes. Hence, the hollow-ring-laser jet-launching platform presented here is complementary to previous jet-launching mechanisms.

Our OMEGA experiment was originally motivated by 2D cylindrical FLASH[8] (https://flash.uchicago.edu) simulations (Fryxell et al. 2000), which showed that a hollow-ring-laser jet can reach much higher density and temperatures along the jet axis due to radial compression and heating of the convergent on-axis flow (Fu et al. 2013), compared to outflows launched by the same laser beams irradiating a single spot on the target. The narrow collimation of these hollow-ring-laser jets was achieved by "inertial confinement" analogous to rocket nozzles, not by radiative collapse. Furthermore, a hollow-ring-laser jet was shown to create and sustain magnetic fields far from the target (Fu et al. 2015). When the ring-shaped blow-off collides along the axis, non-parallel gradients in electron density n_e and electron pressure P_e naturally produce "Biermann battery" (Biermann 1950) magnetic fields along the axis. The larger the hollow ring radius, the stronger the field becomes and the farther it extends from the target (Fu et al. 2015). To demonstrate this hollow-ring-laser magnetized jet concept, we carried out a series of experiments in 2015 and 2016 at the OMEGA laser facility of LLE (Boehly et al. 1995). 20 beams of 500 J each from the upper hemisphere of the OMEGA facility were arranged to form a ring pattern at the flat CH target at laser intensities $>10^{14}$ W cm^{-2} (Figure 1), with ring radius d ranging from 0 to 1200 μm. We used proton radiography (P-rad; Li et al. 2006; Zylstra et al. 2012; Gao et al. 2012) to diagnose the magnetic field, optical Thomson scattering (TS; Mackinnon et al. 2004; Froula et al. 2006; Katz et al. 2012; Follett et al. 2016) to measure the plasma and flow parameters at the target chamber center (TCC; 2.5 mm above target, Figure 1), and time-lapse imaging with an X-ray framing camera (XRFC; Bradley et al. 1995; Benedetti et al. 2012) to image the jet emission. The experimental setup is sketched in Figure 1.

2. Results on Magnetic Fields

The most interesting and important results come from the magnetic field diagnostics. Figure 2 shows raw P-rad images from laser rings of radius $d = 0$, 400, 800, and 1200 μm. As the radius d increases, the magnetic fields appear stronger, more collimated, and extend out further, up to ~5 mm for $d = 1200$ μm. The light and dark patterns, created by proton deflections, correspond to net positive and negative currents

[8] FLASH4 is available at https://flash.uchicago.edu/.

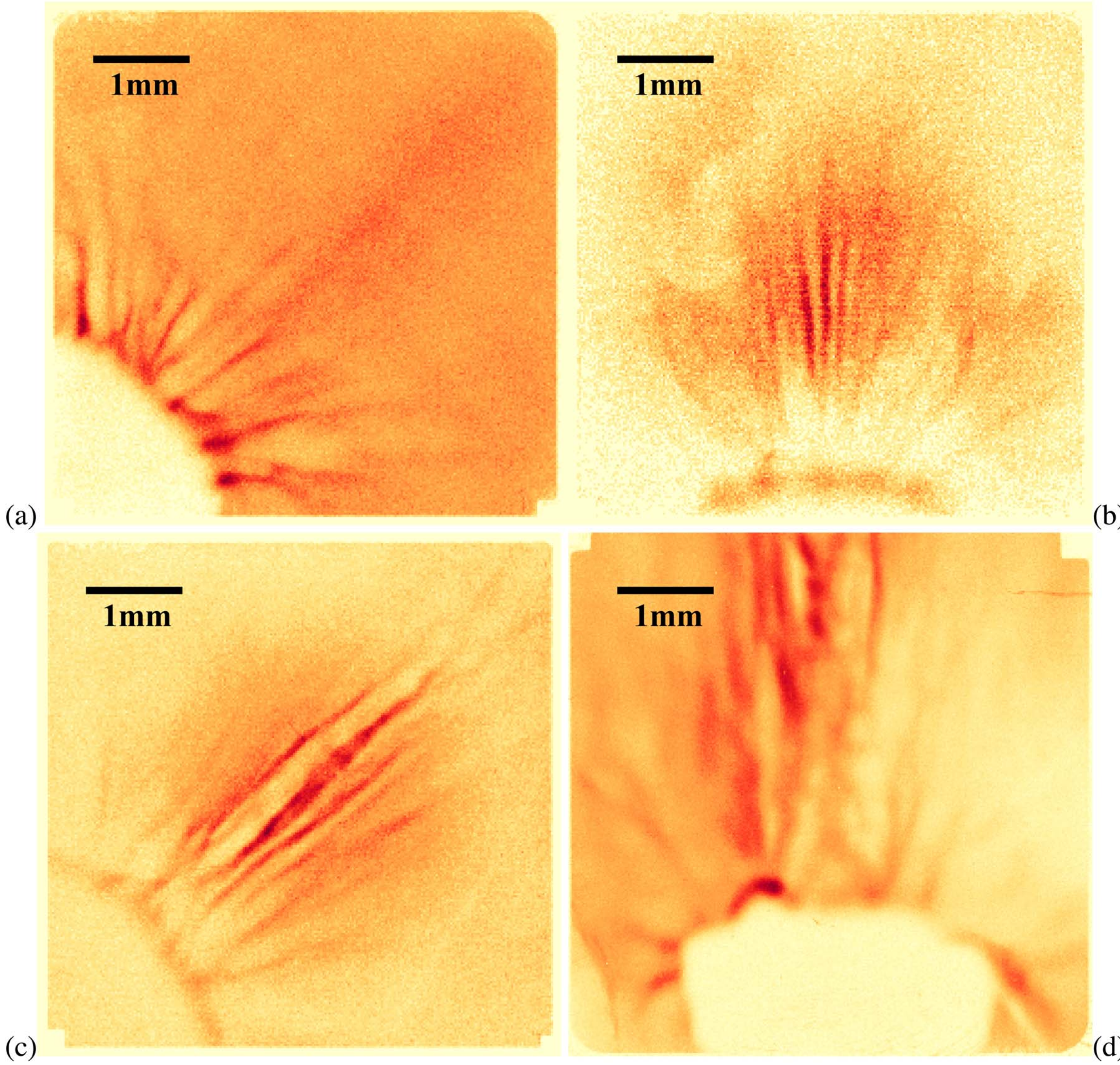

Figure 2. Comparison of P-rad images for jets launched by four different ring-laser radii d: (a) $d = 0$, $t = 3.6$ ns; (b) $d = 400$ μm, $t = 2.6$ ns; (c) $d = 800$ μm, $t = 3.6$ ns; (d) $d = 1200$ μm, $t = 4.3$ ns. All images are those of 14.7 MeV protons. The circular cutoff at the bottom corresponds to the edge of the target.

projected along the line of sight into and out of the plane (Kugland et al. 2012; Graziani et al. 2016; Bott et al. 2017). Vertical proton image filaments correspond to B_z fields, while Y-shaped branches are mainly caused by B_ϕ fields viewed at a slant angle. As the ring radius d is increased, stronger fields are created further from the target and more concentrated along the axis. Even though the 3D magnetic field geometry cannot be uniquely inferred from the 2D proton images, we can still constrain the $\boldsymbol{B}$ field components orthogonal to and integrated along the line of sight, using direct inversion techniques (Graziani et al. 2016; Bott et al. 2017). Figure 3 gives a sample direct inversion result for the transverse $|\boldsymbol{B}|$ of the $d = 800$ μm jet at 3.6 ns along the line-out in blue. Because the physical width of the jet deduced from X-ray images is <1.1 mm, we conclude that the maximum transverse $|\boldsymbol{B}|$ field (central spike in Figure 3(c)) must exceed an MG.

Below we present the simulated P-rad images of the $d = 800$ μm jet using $\boldsymbol{B}$-fields predicted by 3D FLASH simulations. Details of the simulations will be reported elsewhere (Lu et al. 2019). The generalized Ohm's law (Krall & Trivelpiece 1973; Epperlein 1984; Epperlein & Haines 1986) used in the FLASH code includes advection, diffusion, and Biermann battery terms (c = light speed, e = electron charge):

$$\frac{\partial \boldsymbol{B}}{\partial t} = \nabla \times (u \times \boldsymbol{B}) - c\nabla \times (\eta \boldsymbol{j}) + c\frac{\nabla P_e \times \nabla n_e}{e n_e^2} \quad (1)$$

where u = flow advection velocity, η = electrical resistivity, P_e = electron pressure, and n_e = electron density. Figure 4(a) shows $|\boldsymbol{B}|$ profiles at 3 ns predicted by FLASH for four different ring radii d. As d is increased, the maximum field increases and becomes more parallel and concentrated toward the axis, consistent with the P-rad images of Figure 2. The maximum FLASH-predicted fields reach $\sim$MG for $d = 800$ μm and 1200 μm, also consistent with the direct inversion results (Figure 3). Detailed field line plots of the $d = 800$ μm jet (Figure 4(b)) show that they are dominated by poloidal B_z (// to the jet axis) fields near the jet axis and by azimuthal B_ϕ fields (around the jet axis) near the target surface. Figure 4(c) compares the FLASH-simulated P-rad images (left column) with the observed images (right column) at different times, showing good agreement. Both the spacing and contrast of the bright and dark

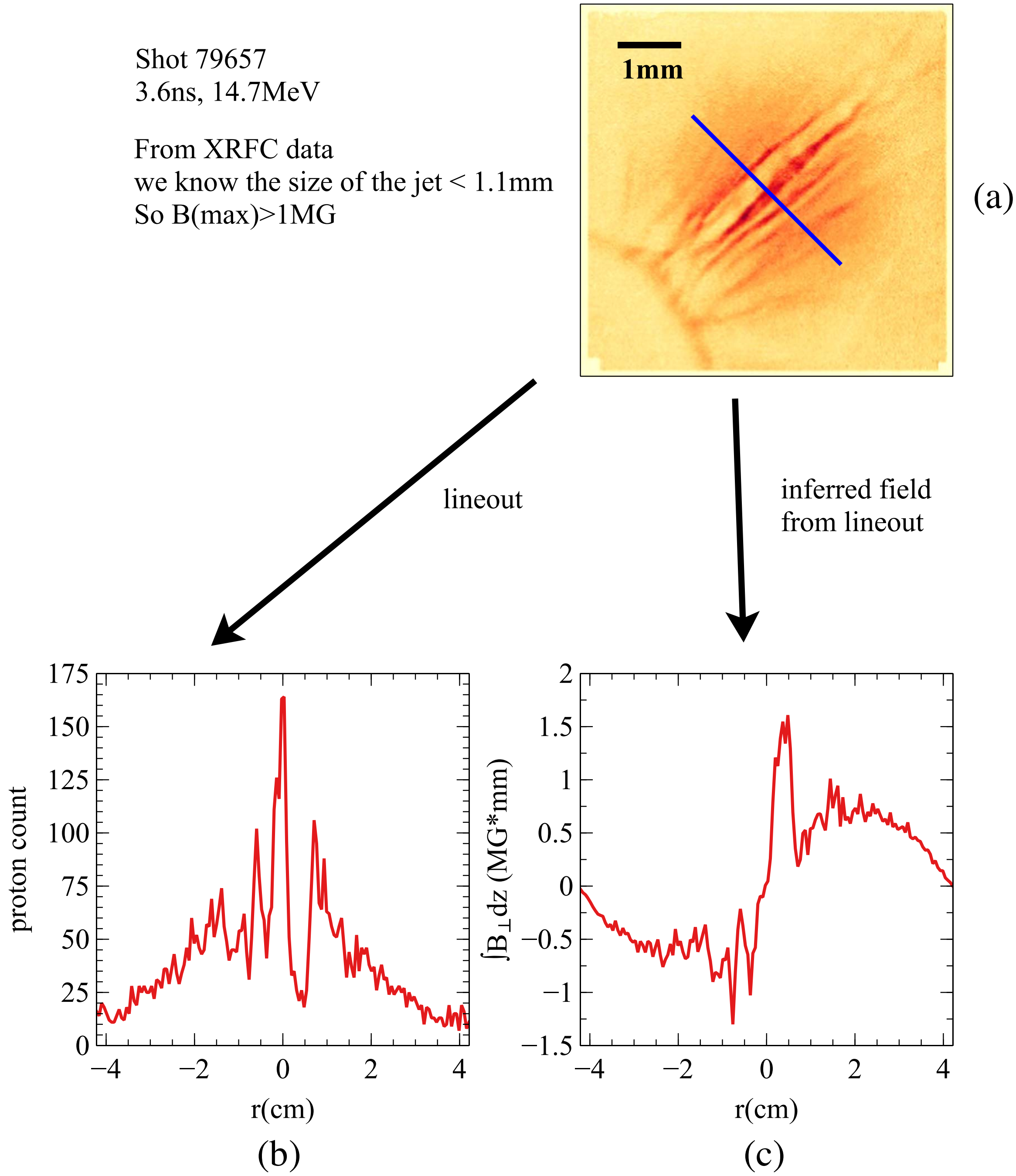

Figure 3. Cross section of integrated transverse $\boldsymbol{B}$-field profile (c) of the $d = 800$ mm jet obtained from the direct inversion of the proton density profile (b), corresponding to the line-out in blue of the P-rad image (a).

streaks, which are sensitive to absolute field amplitudes, are consistent between FLASH simulation and experiment.

Detailed analysis suggests that the primary cause of seed field generation is the collisions between blow-offs from individual laser spots, which create non-parallel density and temperature gradients on the scale of the laser spot radius $r \sim 125\ \mu$m. These filamentary seed fields are then advected toward the jet axis and compressed, producing the strongest fields near the axis (Figures 4(a) and 4(b)). When the ring radius d increases, there is more room for radial advection and compression, leading to stronger and more collimated $\boldsymbol{B}$ fields (Figure 4(a)). At late times, the fields are dominated by a few para-axial bundles with $|B_z| > |B_r|$, $|B_\phi|$ (Figure 4(b)), which result in the proton images that we see in Figures 2 and 4(c). Thus we have demonstrated the creation of cylindrical plasma jets with self-generated MG fields extending to >4 mm along the jet axis. The amplitude and geometry of these fields can be manipulated by dialing the ring radius and laser parameters.

We can obtain order-of-magnitude estimates of the maximum B-field near the jet axis from dimensional analysis using Equation (1), by balancing the advection term with the Biermann battery term, because the diffusion term is negligible in this case. We find $B_{\rm max} \sim ({\rm cd/eu})({\rm k}T_{\rm e}/{\rm r}^2)$, where u = radial advection velocity $\sim$ ion thermal velocity $\sim (kT_{\rm i}/Am_{\rm p})^{1/2}$, k = Boltzmann constant, $\rm m_p$ = proton mass, and $A = 6.5$ for CH. Therefore, $B_{\rm max} \sim {\rm MG}\ \ (d/800\ \mu{\rm m})\ \ (T_{\rm e}/{\rm keV})(T_{\rm i}/A/{\rm keV})^{-1/2}$, in good

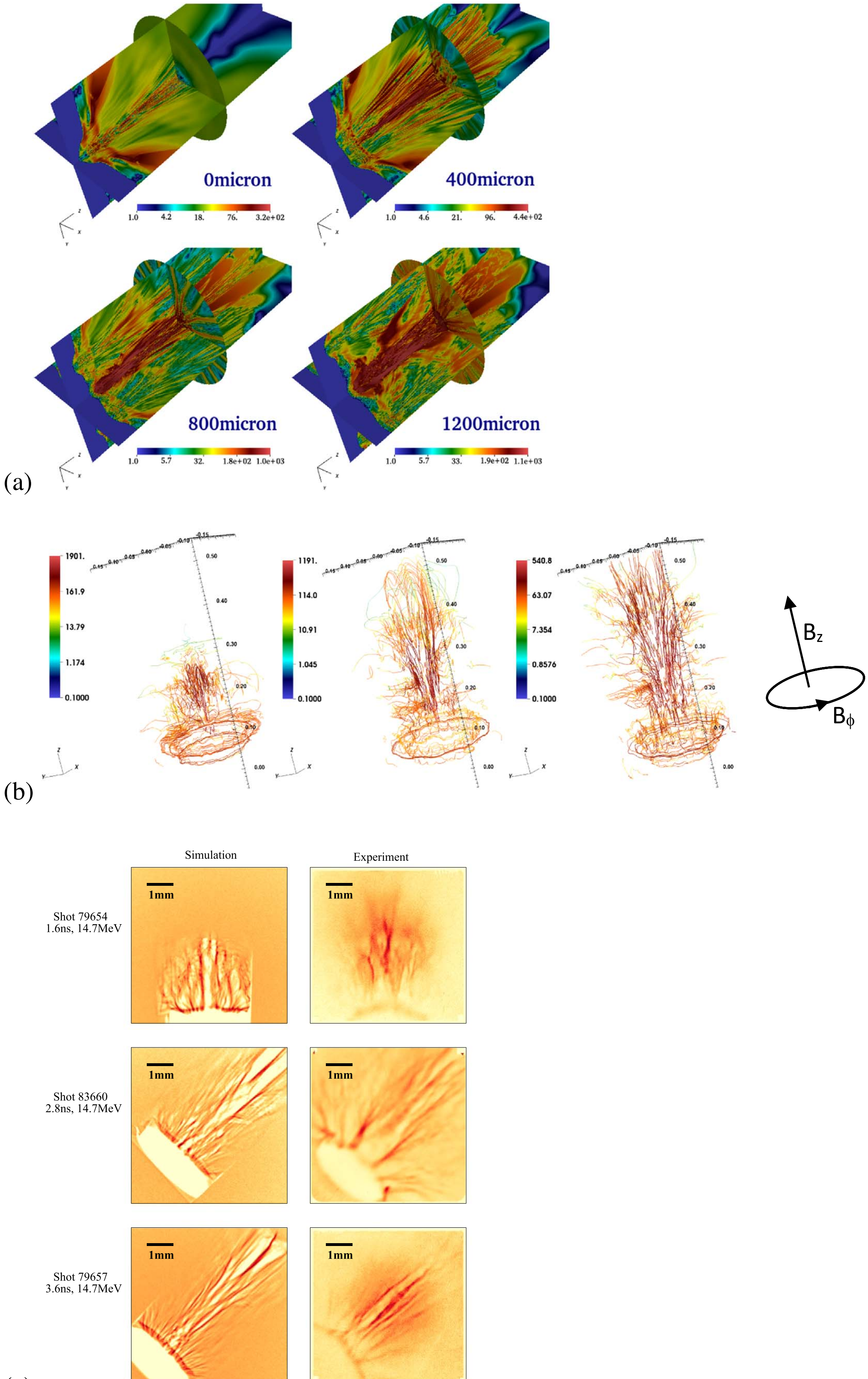

Figure 4. (a) Comparison of 3D FLASH simulations for $|\mathbf{B}|$ profiles at 3 ns for four different ring-jet radii d. (b) Sample field lines at $t = 1.6$ ns, 2.8 ns, and 3.6 ns of the $d = 800$ μm jet. Color scales denote field amplitudes in kG. By symmetry, B_z dominates near the jet axis, while B_ϕ dominates near the target surface. (c) Comparison of 3D FLASH-predicted P-rad images (left column) and observed D^3He P-rad data (right column) for the $d = 800$ μm jet, at the same times as Figure 4(b).

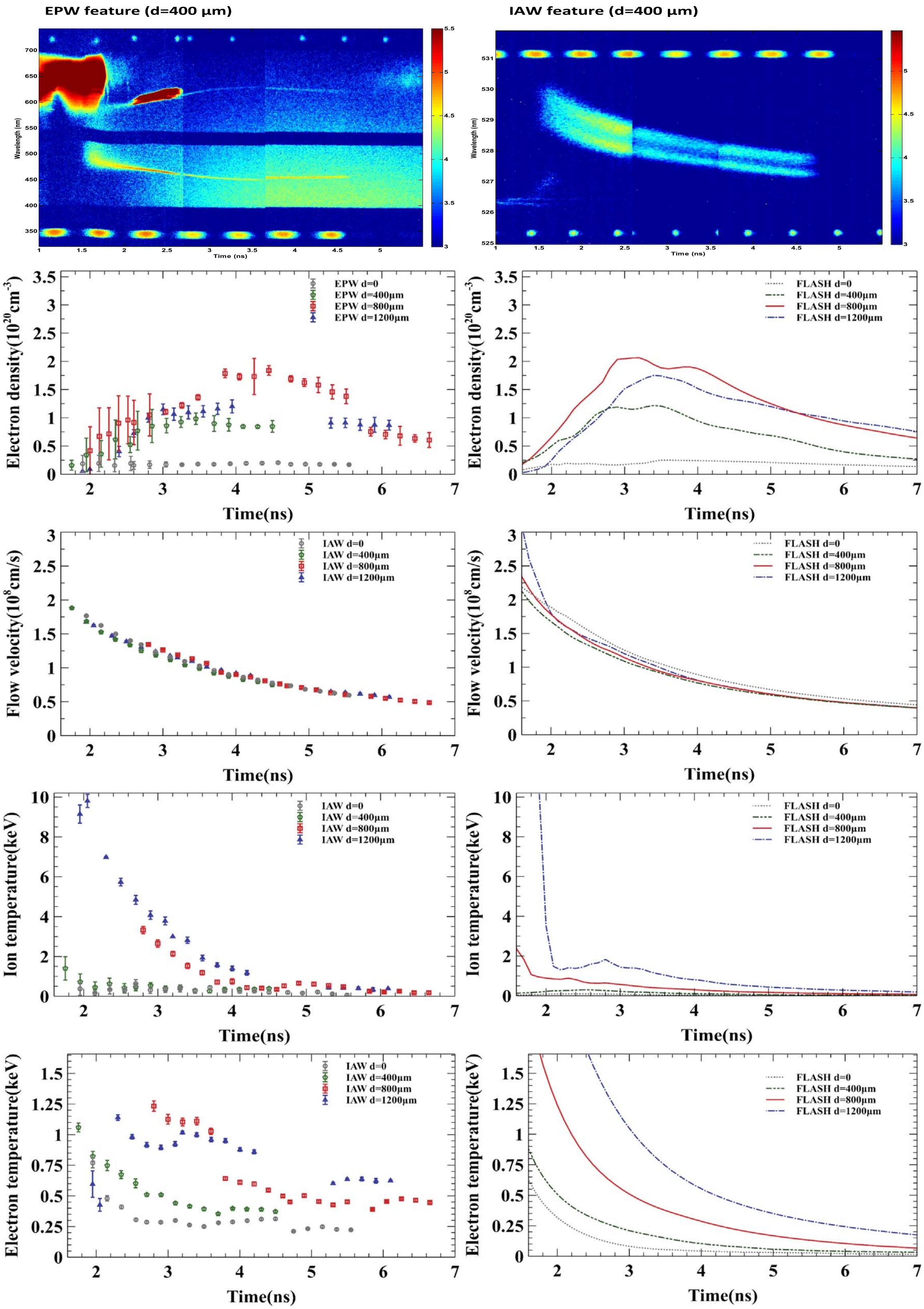

Figure 5. Top row: TS electron plasma wave (EPW) and ion acoustic wave (IAW) spectra vs. time for the $d = 400\ \mu$m jet (combination of 3 shots). Left column, rows 2 to 5: time histories for density, flow velocity, and ion and electron temperatures at TCC for jets of different ring radii d derived from TS spectra. Right column, rows 2 to 5: time histories for density, flow velocity, and ion and electron temperatures at TCC based on 3D FLASH simulations.

agreement with both the direct inversion results (Figure 3) and 3D FLASH predictions (Figure 4(a)). This scaling formula suggests that $B_{\max}$ can be increased by increasing d or T_e (which increases with laser intensity). We also note that in our previous 2D simulations (Fu et al. 2015), because of the assumption of perfect cylindrical symmetry, the only gradient length scale is d. Replacing

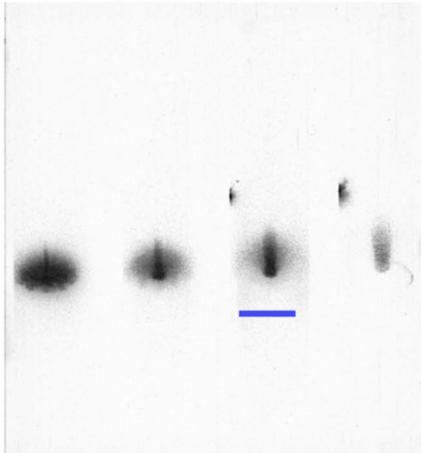

(a)

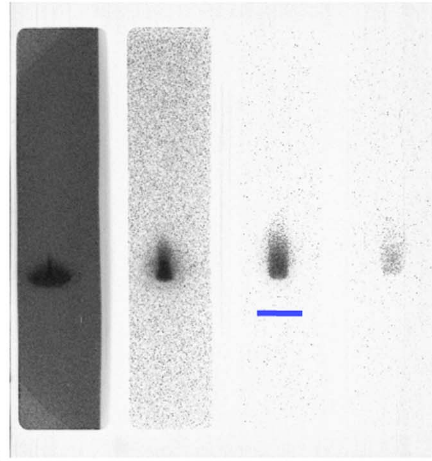

(b)

Figure 6. Time-lapse XRFC images (500 ps exposure) of $d = 800\ \mu$m jets for (a) 2% Fe-doped CH target and (b) pure CH target. In (a) the frames are taken at 2 , 3, 4, and 5 ns. In (b) the frames are taken at 2, 2.5, 3, and 4 ns. The blue marker in each picture denotes a length of 1.6 mm. It is clear that the Fe-doped jet appears narrower than the pure CH jet.

Table 1
Measured Parameters of the $d = 800\ \mu$m jet at 3.5 ns and 2.5 mm from Laser Target On-axis (Left Column) Compared to those of YSO Jets (Right Column)

$d = 800\ \mu$m OMEGA Jet	YSO Jet
Electron density $n_e \sim 1.5 \times 10^{20}$ cm^{-3}	$\sim 10^2$–10^5 cm^{-3}
Electron temperature $T_e \sim 1$ keV	$\sim 10^4$ K-few $\times 10^6$ K
Ion temperature $T_i \sim 2.5$ keV	$\sim T_e$
Ionization $\langle Z \rangle \sim 3.5$	low-100%
Flow velocity $v \sim 1.2 \times 10^8$ cm s^{-1}	$\sim$few $\times 10^7$ cm s^{-1}
Magnetic field $B \sim 10^6$ Gauss	$\sim$20–500 μG
Plasma beta $\beta = 8\pi P_g/B^2 \sim 10$	~ 10–10^3
Mach number $M = v/c_s \sim 3$	few-10
Alfvén Mach number $M_A = v/v_A \sim 8$	$\sim 10^2$
Reynolds number $R_e \sim 10^4$	~ 10–10^3
Magnetic Reynolds number $R_{eM} \sim 10^4$	$\sim$few $\times 10^2$
Peclet number $P_{e\|\|} = 1.5\ kn_e vR/\kappa_{T\|\|B} \sim 0.3$	unknown
$P_{e\ \mathrm{orth}} = 1.5\ kn_e vR/\kappa_{T\ \mathrm{orth}\ B} \sim 30$	unknown
Hydro time/Rad. cooling time (CH) ~ 0.01	various
Hydro time/Rad. cooling time (2%Fe) ~ 1	
Electron skin depth $c/\omega_e \sim 0.4\ \mu$m	
Ion skin depth $c/\omega_I \sim 24\ \mu$m	
Debye length $v_e/\omega_e \sim 0.01\ \mu$m	
Electron gyroradius $v_e/\omega_{Be} \sim 0.6\ \mu$m	
Ion gyroradius $v_i/\omega_{Bi} \sim 20\ \mu$m	
Coulomb scattering mean free path $\lambda_{ei} \sim 20\ \mu$m	

d/r^2 with $1/d$ in the equation above, we obtain $B_{max} \sim 25$ kG for $d = 800\ \mu$m, again in good agreement with 2D FLASH predictions (Fu et al. 2015). The difference in the magnitude of B_{max}, a 2D-cylindrical Biermann battery, can only generate B_ϕ field (Fu et al. 2015), whereas the 3D Biermann battery field is complex and dominated by B_z near the axis (Figure 4(b)). We emphasize that simulated P-rad images using 25 kG pure B_ϕ fields completely disagree with the observed images (Figures 2 & 4(c)).

3. Plasma Parameters and Jet Morphology

The time histories of density, temperatures, and velocity at TCC were measured using optical TS (Mackinnon et al. 2004; Froula et al. 2006; Katz et al. 2012) with a $2\omega_o$ ($\lambda_o = 526.5$ nm) probe beam. Figure 5 compares the experimental data derived from TS with 3D FLASH predictions. The plasma parameters were inferred from the TS spectra from electron plasma waves and ion acoustic waves, using the technique discussed in Follett et al. (2016). Comparing with FLASH predictions, the agreements for electron density and flow velocity are excellent, and the qualitative trends for T_i and T_e are basically consistent. However, we still need to improve the temperature calculations in FLASH to get better quantitative agreement with the temperatures inferred from TS (Lu et al. 2019). Both simulation and experimental data suggest that the $d = 800\ \mu$m jet achieves the highest maximum density on-axis, whereas the $d = 1200\ \mu$m jet achieves the highest maximum temperature on-axis, respectively.

Evolution of the global jet morphology was observed using time-lapse X-ray imaging with an XRFC (Bradley et al. 1995; Benedetti et al. 2012) located at 38° from the jet axis. Figure 6 compares the evolution of two $d = 800\ \mu$m jets, one with 2% Fe-doped CH target (Figure 6(a)), and one with pure CH target (Figure 6(b)). Both jets are well collimated and stable, but the Fe-doped jet appears even narrower than the pure CH jet due to stronger radiative cooling, consistent with FLASH predictions. In principle, these X-ray images can be used to constrain the density and temperature profiles if the X-ray intensities were absolutely calibrated. Unfortunately, absolute calibration of the X-ray cameras was not performed for these experiments due to the lack of times. We plan to do it for future experiments.

4. Discussions and Astrophysical Applications

Our method of creating strongly magnetized cylindrical jets using a ring of multiple laser beams is ideal for scaling up to larger platforms by using more lasers and higher-intensity beams, such as those available at the National Ignition Facility (NIF) at Livermore, California. In terms of magnetic fields, the key advantage of using more laser beams (e.g., up to 64 beams at NIF) is to make the hollow ring pattern larger and more uniform. A larger ring creates stronger fields due to more room for radial compression (see B_{max} formula in Section 2), and a more uniform ring produces larger pitch angle $|B_\phi/B_z|$, because a higher degree of azimuthal symmetry enhances B_ϕ and reduces B_z (see Equation (1)). Future FLASH simulations will quantify the effects of the ring radius and number of laser beams on $|B_\phi/B_z|$, which plays important roles in the stability of the jet (Krall & Trivelpiece 1973). In addition to modeling astrophysical jets, supersonic outflows with well-characterized ordered magnetic fields can be used to study magnetized shocks (Sironi & Spitkovsky 2009), shear boundaries, reconnection, and other plasma processes via interactions with an opposing jet (Park et al. 2012; Ross et al. 2012; Fox et al. 2013; Huntington et al. 2015), ambient media, and external B-fields.

To address the relevance of our ring-laser jets to astrophysical jets, we present in Table 1 representative physical parameters of the $d = 800\,\mu$m ring jet at 3 ns and 2.5 mm from the laser target. As these hydrodynamic jets are kinetic dominated (in contrast to magnetic-dominated or magnetic tower jets driven by pulse power), they are most relevant to the study of young stellar object (YSO) jets (Frank et al. 2014). Table 1 shows that most dimensionless parameters for both types of jets (plasma β, Mach number, Alfvén Mach number, Reynolds number, and magnetic Reynolds number) lie in the same regime, suggesting the scalability of important properties of the hollow-ring-laser jets to the astrophysical regime (Ryutov et al. 1999, 2000). It has been proposed that the stability of some YSO jets may be caused or enhanced by strong poloidal magnetic fields (Albertazzi et al. 2014). Because our hollow-ring-laser jet is created with strong poloidal fields near the axis (Figure 4), it is a useful platform to study the stabilizing effects of strong poloidal magnetic fields on the propagation of YSO jets. As the density, temperature, flow speed, and magnetic field of the ring-laser jet can be varied in a controllable manner by dialing the ring radius and laser parameters, a broad range of YSO jets with matching dimensionless parameters can be studied with such experiments (Frank et al. 2014).

The ring-laser-jet platform can be readily expanded in several new directions. For example, most early laboratory experiments to study YSO jets used metal targets so that radiative cooling dominates the jet collimation and dynamics (e.g., the PALS experiments, see Section 1), whereas radiative cooling was dynamically unimportant in our pure CH jets (Table 1). However, by adding high-Z dopants to our CH target (Figure 6), we can increase radiative cooling (Table 1) to increase the aspect ratio (L/R) of the hollow-ring-laser jet (Figure 6), consistent with previous PALS experiments (Kasperczuk et al. 2006; Nicolaï et al. 2006). Radiative cooling may also reduce the plasma $\beta(=p_{\rm gas}/p_{\rm B})$ to reach the low-β regime, which should lead to interesting new physics. Consequently, the role of radiative cooling in the diversity of YSO jet morphology (Frank et al. 2014) may be studied in the laboratory by varying the high-Z dopant level.

The ring configuration is also ideal for adding angular momentum to the jet by using tilted-tile target surfaces, so that the blow-off from each individual laser spot becomes slanted. Finally, we can replace the flat target with cone-shaped or bowl-shaped targets. Depending on the opening angle of the cone or the curvature of the bowl, the increased convergence of the on-axis flow can potentially lead to even stronger magnetic field, higher density, temperature, and flow speed than the values listed in Table 1, and all these parameters can be varied experimentally by changing the target shape and composition together with ring radius and laser parameters. Comparing the ring-laser jets with jets launched by other platforms, we see that the ring-laser jet parameters have a larger dynamic range. This increased dynamic range should benefit the laboratory study of a broad range of YSO jets.

Another important and novel property of these kinetic-dominated but strongly magnetized jets is their thermal conductivity (Braginskii 1958; Spitzer 2006). Electron transport in these jets becomes highly anisotropic due to the strong fields and small gyroradii (Table 1). As a result, electron heat conduction is suppressed orthogonal to $\boldsymbol{B}$ (Braginskii 1958), but remains Spitzer-like parallel to $\boldsymbol{B}$ (Spitzer 2006), leading to steeper gradient for the electron temperature in the radial direction but less steep gradient in the axial direction (Figure 4(b)). In addition, the Righi-Leduc term can transport electron energy in azimuthal direction and create azimuthal variation of electron temperature. The Nernst term can slow down the B field advection into the hot region (Gao et al. 2015). Future FLASH predictions including anisotropic thermal conduction and Nernst effect should be testable using our TS and XRFC data, plus other diagnostics. The role of thermal conduction is an outstanding unsolved problem in many fields of astrophysics, including YSO jets. Our ring-laser jet can thus provide a new experimental test bed for theories of magnetized thermal conduction relevant to both laboratory and astrophysical plasmas.

This research was supported by DOE NNSA Grant DE-NA0002721. FLASH simulations were performed on Extreme Science and Engineering Discovery Environment (XSEDE), which is supported by National Science Foundation grant number ACI-1548562, and the Argonne Leadership Computing Facility, which is a DOE Office of Science User Facility supported under Contract DE-AC02-06CH11357. Proton radiography was supported in part by DOE Grant No. DE-FG03-09NA29553, No.DE-SC0007168. E.L. and Y.L. acknowledge partial support by LANL/LDRD during the writing of this Letter.

References

Albertazzi, B., Ciardi, A., Nakatsutsumi, M., et al. 2014, Sci, 346, 325
Bally, J., Reipurth, B., & Davis, C. J. 2007, Protostars and Planets V (Tuscon, AZ: Univ. Arizona Press), 215
Benedetti, L. R., Bell, P. M., Bradley, D. K., et al. 2012, RScI, 83, 10E135
Biermann, L. 1950, ZNatA, 5, 65
Boehly, T. R., Craxton, R. S., Hinterman, T. H., et al. 1995, RScI, 66, 508
Bott, A., Graziani, C., Tzeferacos, P., & White, T. G. 2017, JPlPh, 83, 2017
Bradley, D. K., Bell, P. M., Landen, O. L., et al. 1995, RScI, 66, 716
Braginskii, S. I. 1958, JETP, 6, 358
Ciardi, A. (ed.) 2015, in HEDLA X Conf. Proc. 17, High Energy Density Physics,Part A, special issue (Amsterdam: Elsevier)
Epperlein, E. M. 1984, JPhD, 17, 1823
Epperlein, E. M., & Haines, M. G. 1986, PhFl, 29, 1029
Farley, D. R., Estabrook, K. G., Glendinning, S. G., et al. 1999, PhRvL, 83, 1982
Ferrari, A. 1998, ARA&A, 36, 539
Follett, R. K., Delettrez, J. A., Edgell, D. H., et al. 2016, RScI, 87, 11E401
Fox, W., Fiksel, G., Bhattacharjee, A., et al. 2013, PhRvL, 111, 225002
Frank, A., Ray, T. P., Cabrit, S., et al. 2014, in Protostars and Planets VI, ed. H. Beuther et al. (Tuscon, AZ: Univ. Arizona Press), 451
Froula, D. H., Ross, J. S., Divol, L., & Glenzer, S. H. 2006, RScI, 77, 10E522
Fryxell, B., Olson, K., Ricker, F. X., et al. 2000, ApJS, 131, 273
Fu, W., Liang, E., Tzeferacos, P., & Lamb, D. 2015, HEDP, 17, 42
Fu, W., Liang, E. P., Fatenejad, M., et al. 2013, HEDP, 9, 336
Gao, L., Nilson, P. M., Igumenschev, V., et al. 2012, PhRvL, 109, 115001
Gao, L., Nilson, P. M., Igumenschev, I. V., et al. 2015, PhRvL, 114, 215003
Gourdain, P.-A., Blesener, I. C., Greenly, J. B., et al. 2010, PhPl, 17, 012706
Graziani, C., Tzeferacos, P., Lamb, D., & Li, CK. 2017, RScI, 88, 123507
Gregory, C. D., Howe, J., Loupias, B., et al. 2008, ApJ, 676, 420
Hartigan, P. 2013, in HEDLA IX Conf. Proc. 9, High Energy Density Physics, Special Issue, ed. P. Hartigan (Amsterdam: Elsevier)
Huntington, C. M., Fiuza, F., Ross, J. S., et al. 2015, NatPh, 11, 173
Kasperczuk, A., Pisarczyk, T., Borodziuk, S., et al. 2006, PhPl, 13, 062704
Katz, J., Boni, R., Sorce, C., et al. 2012, RScI, 83, 10E349
Krall, N., & Trivelpiece, A. 1973, Principles of Plasma Physics (New York: McGraw Hill)

Kugland, N., Ryutov, D., Plechaty, C., Ross, J., & Park, H. S. 2012, RScI, 83, 101301
Lebedev, S. V., Chittenden, J. P., Beg, F. N., et al. 2002, ApJ, 564, 113
Lebedev, S. V., Ciardi, A., Ampleford, D. J., et al. 2005, MNRAS, 361, 97
Li, C. K., Séguin, F. H., Frenje, J. A., et al. 2006, PhRvL, 97, 135003
Li, C. K., Tzeferacos, P., Lamb, D., et al. 2016, NatCo, 7, 13081
Livio, M. 1999, PhR, 311, 225
Lu, Y., Tzeferacos, P., Liang, E., et al. 2019, PhPl, 26, 022902
Mackinnon, A. J., Shiromizu, S., Antonini, G., et al. 2004, RScI, 75, 3906
Nicolaï, Ph., Stenz, C., Kasperczuk, A., et al. 2008, PhPl, 15, 082701
Nicolaï, Ph., Tikhonchuk, V. T., Kasperczuk, A., et al. 2006, PhPl, 13, 062701
Park, Hye-Sook, Ryutov, D. D., Ross, J. S., et al. 2012, HEDP, 8, 38
Pisarczyk, T., Kasperczuk, A., Krousky, E., et al. 2007, PPCF, 49, B611
Ross, J. S., Glenzer, S. H., Amendt, P., et al. 2012, PhPl, 19, 056501
Ryutov, D., Drake, R. P., Kane, J., et al. 1999, ApJ, 518, 821
Ryutov, D., Drake, R., & Remington, B. 2000, ApJS, 127, 465
Sari, R., Piran, T., & Halpern, J. P. 1999, ApJL, 519, L17
Sironi, L., & Spitkovsky, A. 2009, ApJL, 707, L92
Spitzer, L. 2006, Physics of Fully Ionized Gases (New York: Dover)
Suzuki-Vidal, F., Lebedev, S. V., Bland, S. N., et al. 2011, Ap&SS, 336, 41
Tikhonchuk, V. T., Nicolaï, Ph., Ribeyre, X., et al. 2008, PPCF, 50, 124056
Zylstra, A. B., Li, C. K., Rinderknecht, H. G., et al. 2012, RScI, 83, 013511

Physics of Plasmas ARTICLE scitation.org/journal/php

Numerical simulation of magnetized jet creation using a hollow ring of laser beams

Cite as: Phys. Plasmas **26**, 022902 (2019); doi: 10.1063/1.5050924
Submitted: 3 August 2018 · Accepted: 15 January 2019 ·
Published Online: 4 February 2019

View Online Export Citation CrossMark

Y. Lu,[1,2] P. Tzeferacos,[3] E. Liang,[1] R. K. Follett,[4] L. Gao,[5] A. Birkel,[6] D. H. Froula,[4] W. Fu,[1] H. Ji,[5] D. Lamb,[3] C. K. Li,[6] H. Sio,[6] R. Petrasso,[6] and M. S. Wei[4]

AFFILIATIONS

[1]Department of Physics and Astronomy, Rice University, Houston, Texas 77005, USA
[2]Theoretical Division, Los Alamos National Laboratory, Los Alamos, New Mexico 87545, USA
[3]Department of Astronomy and Astrophysics, University of Chicago, Chicago, Illinois 60637, USA
[4]Laboratory for Laser Energetics, University of Rochester, Rochester, New York 14623, USA
[5]Princeton Plasma Physics Laboratory, Princeton, New Jersey 08540, USA
[6]Plasma Science and Fusion Center, Massachusetts Institute of Technology, Cambridge, Massachusetts 02139, USA

ABSTRACT

Three dimensional FLASH magneto-hydrodynamic modeling is carried out to interpret the OMEGA laser experiments of strongly magnetized, highly collimated jets driven by a ring of 20 OMEGA beams. The predicted optical Thomson scattering spectra and proton images are in good agreement with a subset of the experimental data. Magnetic fields generated via the Biermann battery term are amplified at the boundary between the core and the surrounding of the jet. The simulation predicts multiple axially aligned magnetic flux ropes with an alternating poloidal component. Future applications of the hollow ring configuration in laboratory astrophysics are discussed.

I. INTRODUCTION

Supersonic, well collimated outflows are ubiquitous in many astrophysical systems, such as young stellar objects (YSOs),[1] active galactic nuclei (AGN),[2] and gamma-ray bursts (GRBs).[3] Despite various astronomical observations, theoretical studies, and numerical modelings of astrophysical jets, many fundamental questions remain, e.g., launching mechanism, composition, and morphology of the magnetic field and stability. Magnetic fields permeate the universe, but their origin is not fully understood, especially in astrophysical jets. A variety of ideas have been proposed in which seed magnetic fields could be created. However, this mechanism has only been demonstrated in the laboratory recently.[4,5]

With advances in large laser facilities, scalable laboratory experiments to study astrophysical phenomena have become achievable. Over the years, experiments have been performed to study astrophysics utilizing high-intensity lasers at the OMEGA laser facility at the Laboratory for Laser Energetics (LLE), the National Ignition Facility (NIF) at Lawrence Livermore National Laboratory, and laser facilities in other countries.[6–13] Laboratory produced jets with proper dimensionless parameters may provide an alternative platform to study the jets of astrophysical scales.

A new way of launching high density and high temperature plasma jets using multiple intense laser beams is to utilize the hollow ring configuration as proposed by Fu *et al.*[14,15] It was demonstrated in two dimensional numerical simulations that a bundle of laser beams of given individual intensity, duration, and focal spot size produces a supersonic jet of higher density, temperature, and better collimation if the beams are focused to form a circular ring pattern on a flat target instead of a single focal spot. The Biermann Battery ($\nabla n_e \times \nabla T_e$) term[16] can generate and sustain strong toroidal fields downstream in the collimated jet outflow far from the target surface. Those simulations were carried out in two dimensional cylindrical geometry, where the intensity variation along the ring due to individual laser beams was neglected. Three dimensional simulations are necessary to understand the formation and evolution of the jet in the actual experiments.

The ring jet experiments were designed and carried out on the OMEGA laser facility[17] in 2015 and 2016.[18] We used 20 OMEGA beams to simultaneously irradiate the target forming a ring pattern. Each beam delivers 500 J of energy in 1 ns. In this paper, we aim to use three dimensional FLASH[19] simulations to explain the observed jet parameters in the experiments. Using the magneto-hydrodynamic (MHD) results, we can predict the diagnostic outcomes from first principles. In Sec. II, we describe the experimental design to produce laboratory jets on the OMEGA laser and the simulation methods to model the experiment. Simulation results are discussed in Sec. III. The validation against a subset of experimental data is discussed in Sec. IV.

II. SIMULATION METHODS

A. Non-ideal magneto-hydrodynamics in the FLASH code

The FLASH code[20] is used to carry out the detailed physics simulations of our laser experiments to study the formation and dynamics of the jet and the origin of magnetic fields. FLASH[19,21] is a publicly available, multi-physics, highly scalable parallel, finite-volume Eulerian code and framework whose capabilities include adaptive mesh refinement (AMR), multiple hydrodynamic and MHD solvers, and implicit solvers for diffusion using the HYPRE library and laser energy deposition. FLASH is capable of using multi-temperature equation of states and multi-group opacities. Magnetic field generation via the Biermann battery term has been implemented and studied in FLASH recently.[22]

We use the same FLASH code units as in Ref. 4 to solve the three-temperature non-ideal MHD equations. A cartesian grid with ($256 \times 256 \times 512$) zones is used to resolve a (3 mm $\times$ 3 mm $\times$ 6 mm) domain, corresponding to $\sim$11 μm per cell width. The number of cells we use is sufficient to resolve the spatial distribution of all the quantities that the plasma diagnostics are able to resolve in the OMEGA experiments. We did test runs at different resolutions and the simulation converged at a cell width of 11 μm. The plasma has zero initial magnetic field. The laser target is modeled as a 3 mm diameter and 0.5 mm thick disk with the composition listed in Table I. To model the material properties of the CH and CH+dopant targets, we utilize the opacity and EoS tables computed with PROPACEOS.[23] We use the equation of state of helium in the chamber with an initial density equal to 2×10^{-7} g/cc, which should have been vacuum. The helium does not affect the simulation significantly, as the mass, momentum, and energy budget in the modeled helium is much less than 1%. To suppress the magnetic field from the numerical artefact, we turn off the Biermann battery term and use the largest allowed magnetic resistivity in the explicit solver for each time step in the regions with a density lower than 2×10^{-5} g/cm^3. The electron heat conduction is calculated using the Braginskii model[24] in a weak magnetic field limit.

To model the laser driven blowoffs, we use the spatial and temporal specifications of each of the twenty OMEGA driver beams. The 20 driver beams are turned on and turned off simultaneously with a 1 ns pulse duration. Each delivers 500 J of energy on a target flat-top. The radius of each beam is 125 μm. The laser spots are arranged to form a ring pattern of radius d, as shown in Fig. 1. The target is 0.5 mm thick to prevent the burn-through. The setup of the diagnostics is sketched in Fig. 2 and discussed in Secs. II B and II C.

TABLE I. Target characteristics used in the experiments and the simulations.

Composition (number fraction)	Density	Laser target ring radius
C(50%) H(50%)	1.04 g/cc	0, 400, 800, 1200 μm
C(49%) H(49%) Fe(2%)	1.21 g/cc	800, 1200 μm

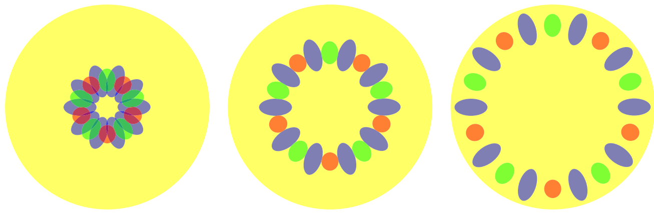

FIG. 1. The illuminated area on the target by 20 OMEGA beams. The transverse sections of the beams are circles, but the spots on the target surface are ellipses due to inclination. The incident angle is 59° for the blue spot, 42° for the green spot, and 21° for the red spot. (a) $d = 400\,\mu$m ring radius; (b) $d = 800\,\mu$m ring radius; (c) $d = 1200\,\mu$m ring radius. The $d = 0$ case is not shown. Note that the red and green spots form a 5-fold symmetry, and the blue spots form a 10-fold symmetry.

For convention, $t = 0$ is the time for laser turn on. The z direction is perpendicular to the surface of the target plane. The jet is formed in the $z > 0$ region. We also use cylindrical coordinates, where $r = 0$ is the central axis of the target. The target surface is located at $z = 0$. The axial direction is along the z axis. The toroidal or azimuthal direction is the φ direction in the cylindrical coordinate system. The target chamber center (TCC) is at $x = y = r = 0$, $z = 0.25$ cm.

B. Optical Thomson scattering

Optical Thomson scattering[25,26] is used to probe the electron/ion temperatures, electron density, and flow velocity at TCC. We used one probe beam with a pulse of 1 ns, an energy of

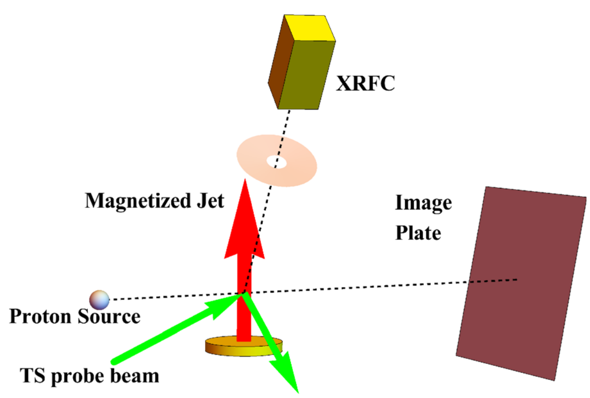

FIG. 2. Schematics of the diagnostics setup of OMEGA magnetized jet experiments. For DD and D^{3}He protons, the source stands 1 cm from TCC, while the image plate CR39 is located 17 cm from TCC on the other side. For the TNSA protons, the source stands 0.8 cm from TCC, while the radiochromic film pack is located 16.5 cm from TCC on the other size. The X-ray framing camera (XRFC) images the jet at 38° from the axis, which is not modeled in this work.

25–50 J, and a wavelength (2ω) of 532 nm as the backlighter. The intensity distribution of the probe beam is 70 μm FWHM 2D Gaussian.

We model the Thomson scattering spectrum using the 3D FLASH simulation results. The spatial profiles of electron density, electron/ion temperature, flow velocity, and mass fraction of species are taken as the input for the spectroscopy code.[27] The heating by the probe beam is modeled by laser absorption. The dispersion relations for the ion acoustic wave and the electron plasma wave[27] are used to calculate the power output. The final power output is weight averaged by the spatial intensity distribution of the probe laser. The instrument broadening[28] is taken into account in the modeling spectrum.

The experimental data are also fitted using the model (see more results in Ref. 18) to compare with the plasma quantities averaged (200 μm)^3 cube centered at TCC.

C. Proton radiography

Our OMEGA experiments used two types of proton sources to map out the magnetic fields (1) DD (3 MeV) and D^{3}He (14.7 MeV) protons from fusion reaction driven by 24 OMEGA beams.[29,30] The actual spectrum is typically an up-shifted symmetric Gaussian distribution, FWHM = 320 keV centered at 3.6 MeV for DD protons and FWHM = 670 keV centered at 15.3 MeV for D^{3}He protons. The emitting position of protons follows a 3D Gaussian distribution with an e-fold radius equal to 20 μm, and the burn time is 150 ps;[30] (2) Broadband protons up to 60 MeV are driven by an OMEGA EP beam via the Target Normal Sheath Acceleration (TNSA) mechanism.[31] The actual spectrum is typically an exponential distribution with an effective temperature of 3.79 MeV for our copper backlighter target.[32] The initial position of protons at the source follows a 3D Gaussian distribution with an e-fold radius equal to 5 μm,[30] and the pulse duration is 1 ps. For the DD and D^{3}He protons, the source stands 1 cm from TCC, while the image plate CR39 is located 17 cm from TCC on the other side. For the TNSA protons, the source stands 0.8 cm from TCC, while the radiochromic film pack is located 16.5 cm from TCC on the other side.

The modeling for proton radiography is composed of (1) sampling for the source distributions mentioned above, (2) solving the trajectory of the protons, and (3) recording the protons on the detector plane.

The deflection of protons in electromagnetic fields is calculated by solving the Newton-Lorentz equation

$$\frac{d(m_p \boldsymbol{v})}{dt} = e\left(\mathbf{E} + \frac{\boldsymbol{v}}{c} \times \mathbf{B}\right). \tag{1}$$

In a typical MHD fluid, $E \approx \frac{v_h}{c} B$, where v_h is the hydrodynamical velocity scale of the fluid. The ratio of electric force to magnetic force is $\frac{E}{(v_p/c)B} \approx \frac{v_h}{v_p}$. For a proton with energy larger than ~MeV, the proton speed v_p is much larger than v_h, so we use electric field $\mathbf{E} = 0$ approximation in the modeling. The energy lost is calculated throughout the proton motion from the NIST PSTAR table.[33] Protons lose a significant amount of energy in the remaining solid target with the density of ~1 g/cc.

We assume that the detector for DD protons has uniform sensitivity for protons with $E > 2$ MeV and that for D^{3}He protons has uniform sensitivity for all protons with $E > 14.4$ MeV. The TNSA proton energy range that each film is primarily sensitive to is $E > E_0$, and the deposited energy per proton is proportional to $(E - E_0)^{-1/2}$, while no energy is deposited for $E < E_0$. The characteristic energy E_0 is different for each pack in the radiochromic film. Temporal smearing of TNSA proton images is neglected because the pulse duration is short. Temporal smearing of DD and D^{3}He protons is calculated using the integral of the second order interpolation among successive images with 0.1 ns intervals.

III. FLASH SIMULATION RESULTS

A. Hydrodynamics

The jet is formed by the merging of the plasma plumes produced by 20 individual OMEGA beams through a strong cylindrical shock. By using a large ring radius, the flows will not collide immediately while the lasers irradiate the target. For the collision at later time with more available room, the flows develop larger radial velocities which become more supersonic. Thus, a stronger cylindrical shock is generated near the z axis. For the cylindrical shock, the surrounding is in the upstream region, and the central core is in the downstream region. It is a hydrodynamic shock where the plasma β is much larger than unity. Figure 3 shows the time evolution of the jet for $d = 800$ μm CH target simulation. The jet is supersonic and well collimated. The jets with different ring radii all travel several millimeters by $t = 3$ ns. The jet keeps traveling and expanding so that the length L and the radius R keep growing even after 3 ns. The width and the length of the jet are much larger than the laser spot size (250 μm), as shown in Table II.

The properties of the jet become more interesting as the ring radius d increases. Figure 4 shows the shape of the jet for different laser ring radii at $t = 3$ ns. Figure 5 shows the evolution of electron/ion temperature, electron density, and flow velocity at TCC for different runs in the FLASH simulation. The quantities are calculated by averaging over a (200 μm)^3 cubic around TCC ($r = 0$, $z = 0.25$ cm). The peak electron/ion temperature on-axis is higher for a larger ring radius. Compared to the case where $d = 0$, the temperatures for $d = 800$ μm or $d = 1200$ μm are about one order of magnitude higher. The peak electron density is the highest for $d = 800$ μm, which is one order of magnitude higher than the $d = 0$ case. The ratio L/R of the jet becomes larger (see Table II) as d gets larger. A large ring radius also reduces the opening angle of the jet. The flow velocity is hardly affected by increasing d. These results are in good agreement with previous 2D cylindrical hydrodynamic simulations by Fu *et al.*[14] using 2D FLASH. The simulations in this work are in 3D cartesian geometry. The full details of the laser configuration are taken into account. In 3D simulations, even though there is the azimuthal asymmetry of the laser intensity on the target as shown in Fig. 1, the jet is still well collimated and has similar hydrodynamical properties to those in the 2D cylindrical case. The azimuthal asymmetry level for electron density can exceed 10%, and the pattern of density distribution in z-slice resembles a "sun flower" as shown in Fig. 7.

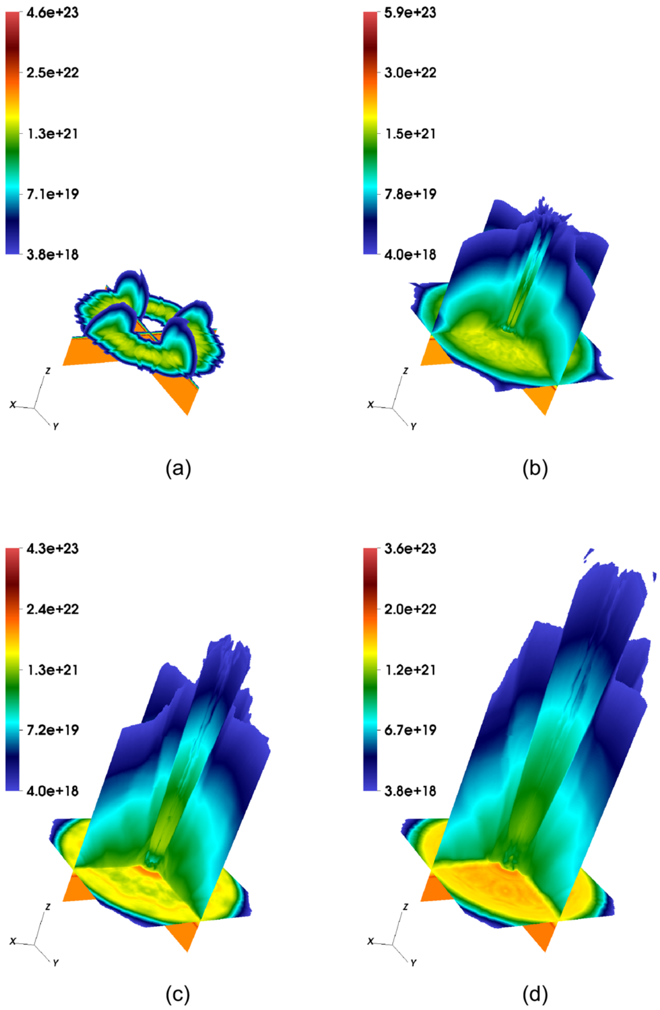

FIG. 3. Three-slice plots for electron density at $x = 0$, $y = 0$, and $z = 0.01$ cm planes in FLASH simulations. The unit is cm^{-3}. The $z = 0.01$ cm plane in the simulation is $(0.3\,\text{cm})^2$ rectangle. The ring radius is $d = 800\ \mu$m, and the target is CH. (a) $t = 0.6$ ns (when laser is still on), (b) $t = 1.4$ ns (0.4 ns after the laser is turned off), (c) $t = 2.2$ ns, and (d) $t = 3.0$ ns. These plots show the time evolution of the jet.

The jet for the 2% Fe dopant shot is slightly different from the one without the dopant, as shown in Fig. 6. The jet in a dopant shot radiates several times more than that in a non-dopant shot. But the radiative cooling time at $t = 3$ ns for the jet is much larger than nanosecond even in the dopant shot. Thus, the radiation cooling (see Table III) has little to do with the shape of the jet after it has grown to millimeter size. For an earlier time, however, the cooling rate is large enough to play a role. As a result, the electron temperature at TCC for doped jets is always lower than that for non-doped jets with the same ring radius d. The reduction in electron temperature relaxes the cylindrical shock. Thus, more electrons flow into the core, which causes the jets in dopant shots to have higher electron density than the non-dopant ones. In both doped and non-doped cases, the jets are always optically thin.

A list of on-axis plasma properties from a snapshot in FLASH simulation results is listed in Table IV using the snapshot for the $d = 800\ \mu$m case at $t = 3$ ns. Other relevant physical terms can be deduced from the scales and dimensionless numbers in Table IV. The plasma in the jet is fully ionized, i.e., $A = 6.5$ and $Z = 3.5$ for non-doped shots and $A = 7.49$ and $Z = 3.95$ for doped shots. The optical Thomson scattering diagnostics are simulated and discussed in Sec. IV A. By including laser energy deposition from the probe beam, the hydrodynamical variables in a small region of around $(100\ \mu\text{m})^3$ will change significantly. This effect is significant for the analysis of diagnostics but not of main interest in the dynamical evolution of the jet.

B. Magnetic fields

Without any initial magnetic fields, the seed magnetic field is generated via the Biermann battery term caused by the individual beam heating. The azimuthal asymmetry in the system is significant for the generation of seed fields. In Table IV, the Hall number Ω_H is much larger than the Biermann number Bi. The Hall term is zero if $\mathbf{B} = 0$, so it does not generate seed fields. Thus, the Hall term $[-\frac{c}{e}\nabla \times \frac{(\nabla \mathbf{B})\times\mathbf{B}}{4\pi n_e}]$ is neglectable in our system. The Biermann battery term is the only source term in the generalized Ohm's law that we calculate in FLASH simulation. Magnetic resistivity is also included in the computation. However, due to the large magnetic Reynolds number, magnetic reconnection can hardly happen until later on in the MHD picture.

TABLE II. Comparison of plasma properties for different ring radii and targets at $t = 3$ ns and $r = 0$, and $z = 2.5$ mm. n_e, ρ, T_e, T_i, and B are calculated by averaging over a $(200\ \mu\text{m})^3$ cubic around TCC. The jet length L is the defined by the point on the z axis where electron density drops to 3×10^{18} cm^{-3}. Radius R is defined by reading the position in the $z = 2.5$ mm plane where the density scale height $|\nabla \log \rho|^{-1}$ reaches the minimum. Columns 2 to 5 are for pure CH targets. Columns 6 and 7 are for 2% Fe dopant targets.

Plasma property	$d = 0$	$d = 400\ \mu$m	$d = 800\ \mu$m	$d = 1200\ \mu$m	$d = 800\ \mu$m 2% Fe dopant	$d = 1200\ \mu$m 2% Fe dopant
Electron density n_e (cm^{-3})	1.7×10^{19}	1.2×10^{20}	2.0×10^{20}	1.5×10^{20}	2.7×10^{20}	1.6×10^{20}
Electron temperature T_e (eV)	81	2.1×10^2	5.1×10^2	1.0×10^3	3.9×10^2	8.5×10^2
Ion temperature T_i (eV)	76	2.2×10^2	5.7×10^2	1.4×10^3	5.9×10^2	2.4×10^3
Magnetic field B (gauss)	2.4×10^4	1.4×10^5	3.3×10^5	3.1×10^5	3.5×10^5	3.7×10^5
Jet width R (cm)	>0.15	0.091	0.049	0.039	0.047	0.042
Jet length L (cm)	0.46	0.52	0.54	0.53	0.55	0.50
L/R	<3.1	5.7	11	13.6	11.7	11.9

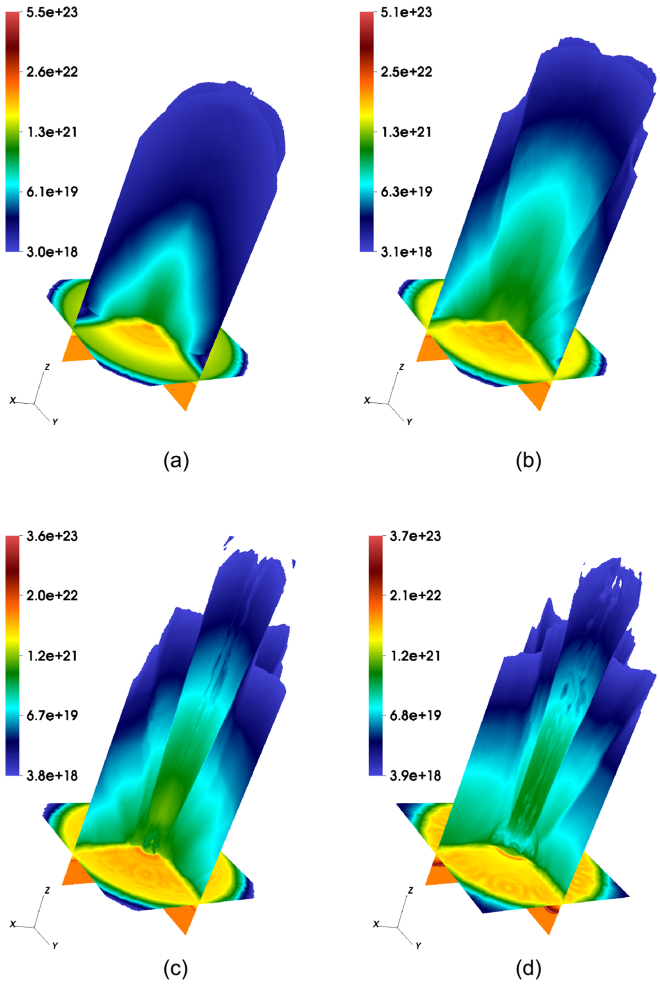

FIG. 4. Three-slice plots for electron density at $x = 0$, $y = 0$, and $z = 0.01$ cm planes at $t = 3$ ns for four different ring radii d in FLASH simulations. The unit is cm^{-3}. The scale is the same as in Fig. 3. The targets are CH. (a) $d = 0$, (b) $d = 400\ \mu$m, (c) $d = 800\ \mu$m, and (d) $d = 1200\ \mu$m. (c) is the same as Fig. 3(d).

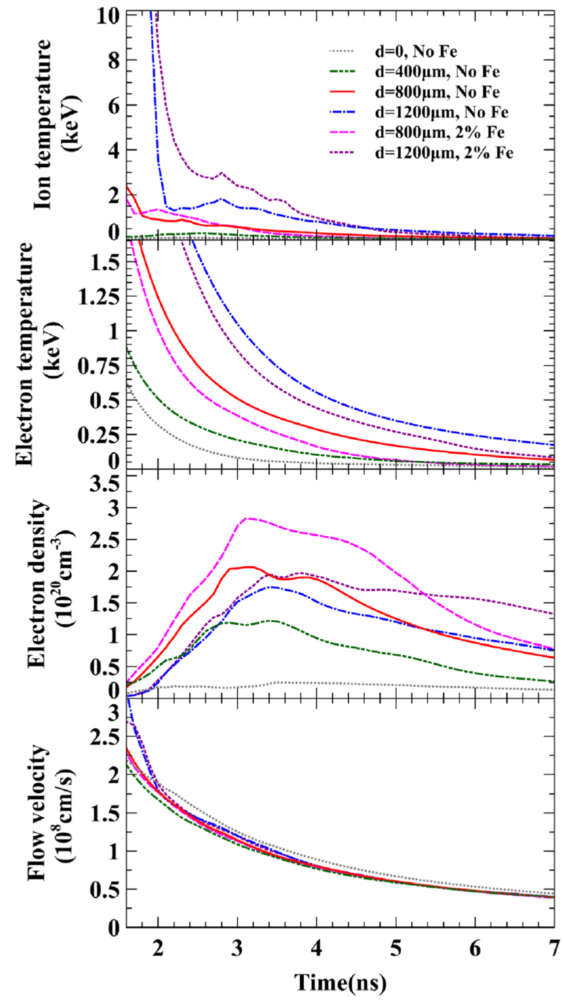

FIG. 5. The evolution of plasma variables at TCC for the six different runs in FLASH simulation. Four sub-figures share the time axis and legends. The quantities are calculated by averaging over a $(200\ \mu m)^3$ cubic around TCC.

The generation and evolution of the axial dominant magnetic field are demonstrated in Fig. 7. Because of the radial temperature gradient [see Fig. 7(a)] and the azimuthal density gradient [see Fig. 7(b)], the Biermann battery term ($\frac{c}{e}\nabla \times \frac{\nabla P_e}{n_e} = \frac{ck_B}{e}\nabla T_e \times \nabla n_e$) is mainly in the axial direction. Toroidal dominated magnetic fields are only generated near the surface of the target, where there is a little azimuthal density gradient but a large axial density gradient. At a millimeter above the target surface, the magnetic field is generated in the surrounding [the ring near $r \approx 0.08$ cm in Fig. 7(c)] and advected into the core [the central part of Fig. 7(d)]. The shock amplifies the axial magnetic field by a factor of $\sim$4 due to the flux conservation as the plasma flows from the surrounding to the core. The cylindrical shock makes the magnetic field highly concentrated as shown in Fig. 7(e). Because the gradient of density alternates several times azimuthally, the generated axial field also alternates. The 5-fold symmetry in the field comes from the 5-fold symmetry in arranging the laser spots as shown in Fig. 1. The symmetry is slightly broken in the simulation due to the cubic cells and finite resolution. By using a larger ring of laser spots, the magnetic energy is more concentrated in the core of the jet as shown in Figs. 9 and 10.

The magnetic field is mostly axial near the z axis and mostly toroidal near the surface of the target, as shown in Figs. 7(f) and 8. The width and the length of the field bundles grow with the jet. The maximum field strength reaches several hundred kilogauss. The maximum magnitude of the magnetic field at $t = 3.6$ ns increases with the radius d of the laser ring, as shown in Fig. 10. This is consistent with the 2D cylindrical simulation.[15] However, the full three dimensional simulation predicts a magnetic field axial polarized and much stronger than that in the two dimensional cylindrical simulation. In the 2D cylindrical simulation, the laser intensity is azimuthally uniform, and thus, the Biermann battery term only has the toroidal component.

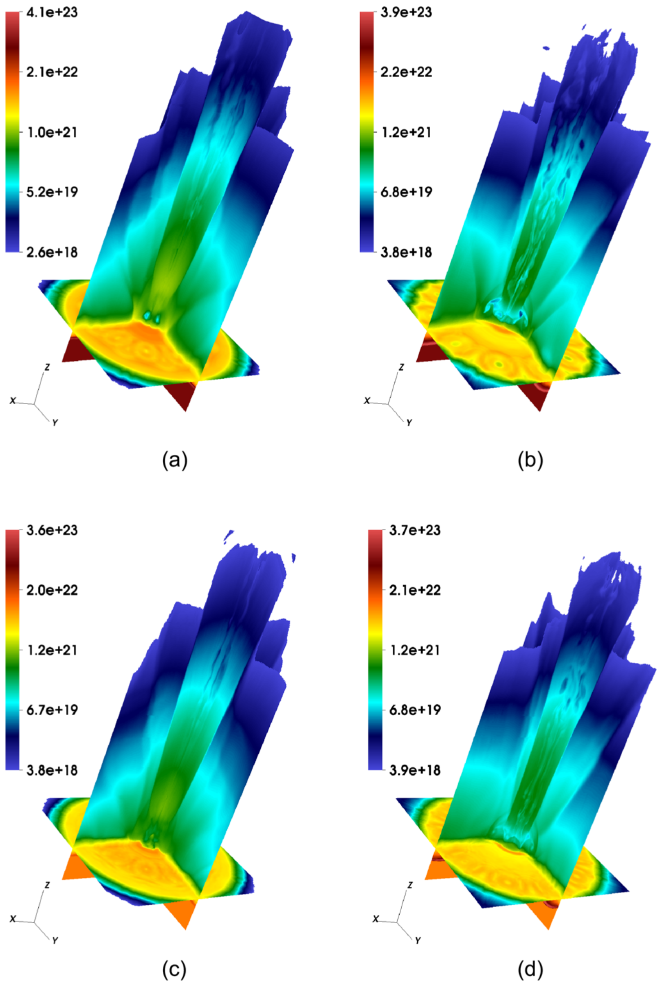

FIG. 6. Three-slice plots for electron density (unit: cm^{-3}) at $x = 0$, $y = 0$, and $z = 0.01$ cm planes at $t = 3$ ns for two different ring radii d and for two different types of targets in FLASH simulations. The unit is cm^{-3}. The scale is the same as in Fig. 3. (a) $d = 800\,\mu$m, 2% Fe-doped target, (b) $d = 1200\,\mu$m, 2% Fe-doped target, (c) $d = 800\,\mu$m, CH target, and (d) $d = 1200\,\mu$m, CH target. (c) is the same as Fig. 4(c), and (d) is the same as Fig. 4(d).

IV. DIAGNOSTICS MODELING AND COMPARISON TO EXPERIMENTS

A. Optical Thomson scattering spectrum

Although we can fit the optical Thomson-scattering spectrum using the theoretical spectrum to infer the temperatures, density, and flow velocity, the gradient of these quantities near TCC can affect the spectrum and mislead the interpretation. As shown in Table IV, the variation of some quantities can exceed 10% and thus significantly alters the spectrum. Moreover, the 2ω probe beam can potentially heat the plasma near TCC. In our simulation, the heating effect and all the gradients are taken into account. Instead of directly comparing the deduced quantities with those predicted in Fig. 5, we compare the synthetic spectrum with the data for the experimental spectrum in Fig. 11.

TABLE III. Radiation properties of the jet at TCC for $d = 800\,\mu$m ring radius. The temperature and density are in Table II.

Plasma property	Formula	Value
Planck opacity κ_P (cm^2/g) for CH target	from PROPACEOS	1.8×10^{-2}
Optical depth τ for CH target	$\kappa_P \rho L$	1.1×10^{-6}
Cooling rate (1/s) for CH target	$0.72AZ^{-1}\kappa_P T_e^3$	3.2×10^{6}
Planck opacity κ_P (cm^2/g) for 2% Fe dopant target	from PROPACEOS	3.9×10^{-1}
Optical depth τ for 2% Fe dopant target	$\kappa_P \rho L$	4.4×10^{-6}
Cooling rate (1/s) for 2% Fe dopant target	$0.72AZ^{-1}\kappa_P T_e^3$	3.2×10^{7}

Figures 11(a) and 11(b) show that the heating from the TS probe has a significant impact on the measured spectra. Although the energy in the probe beam (25–50 J) is low compared to the drive beams, the 70 μm diameter focal spot results in an intensity of 10^{15} W/cm^2. FLASH simulations are performed with and without the probe beam to study the impact of probe-beam heating. The locations of the TS peaks in the simulated spectra that included the probe beam are in much better agreement with the measured spectra. The effect is more pronounced for smaller ring radii because the electron temperature is lower, which leads to higher collisional absorption.

The background of the measured EPW spectrum comes from the bremsstrahlung radiation, which is not calculated in the simulation. The bremsstrahlung shape is apparent when the electron density is larger than $\sim 10^{20}$ cm^{-3}.

The agreement for the IAW spectrum is excellent for $d = 0$ when the heating is included, as shown in the first plot in Fig. 11(b). However, for finite d, the simulation always underestimates the width of the broadened line. The depth of the valley in the middle of the shape is corrected by including the heating effect, which can be explained by the increase in the electron temperature from probe heating. The under-predicted width of the IAW spectrum indicates the under-predicted ion temperature. Because ions are not directly heated by the probe beam, we also compare the ion temperature from fitting the IAW spectrum and the $(200\,\mu m)^3$ averaged value in FLASH simulations in Fig. 12.

One may argue that the reason for underestimating the IAW line width is the inaccuracy of the RAGE-like (it is so named because it is identical to the method implemented in the radiation hydrodynamic code RAGE[34]) energy apportion in our modeling. The RAGE-like approach apportions the work term among the ions, electrons, and radiation field in proportion to the partial pressures of these components. It is physically accurate in smooth flow but does not distribute internal energy correctly among the ions, electrons, and radiation field at shocks. For the finite d case, strong and multiple shocks are presented. There are the shocks between the plumes generated by neighboring beams and the cylindrical shock surrounding the core. The core is usually a secondary downstream. The ion heating exists at all shocks but is not calculated accurately using the RAGE-like approach. The electron temperature should be significantly overestimated if the energy apportion between electrons and ions is inaccurate. However, the comparison between the measured IAW spectrum and the synthetic spectrum with probe heating does not suggest any significant overestimation of

TABLE IV. Simulated plasma properties for case $d = 800\,\mu$m, $t = 3$ ns at $z = 2.5$ mm in non-dopant run. All quantities are in cgs units except temperatures expressed in eV. The length scale is L approximately the width of the jet at $z = 2.5$ mm, which is $L \approx 1$ mm. n_e, ρ, T_e, and T_i at $r = 0$ are calculated by averaging over a $(200^3\,\mu\text{m})^3$ cubic around TCC. n_e, ρ, T_e, and T_i at $r = 1$ mm are calculated by averaging over a 200 μm high and 200 μm thick ring around $r = 1$ mm, $z = 2.5$ mm. B is calculated using the root of mean square in the same cubic. The variation of n_e is $\Delta n_e = \sqrt{\overline{n_e^2} - \overline{n_e}^2}$, similar for other variables.

Plasma property	Formula	Value at $r = 0$	Value at $r = 1$ mm
Electron density n_e (cm^{-3})	...	2.0×10^{20}	3.0×10^{19}
Δn_e (cm^{-3})	...	1.5×10^{19}	4.1×10^{18}
Mass density ρ (g/cm^3)	...	6.3×10^{-4}	1.1×10^{-4}
$\Delta\rho$ (g/cm^3)	...	4.7×10^{-5}	1.3×10^{-5}
Electron temperature T_e (eV)	...	5.1×10^2	3.9×10^2
ΔT_e (eV)	...	1.2	1.4
Ion temperature T_i (eV)	...	5.7×10^2	1.8×10^2
ΔT_i (eV)	...	1.2×10^2	17
Magnetic field B (gauss)	...	3.3×10^5	4.6×10^4
ΔB (gauss)	...	1.5×10^5	3.0×10^4
Average ionization Z	...	3.5	3.5
Average atomic weight A	...	6.5	6.5
Flow velocity $u \approx u_z$ (cm/s)	...	1.1×10^8	1.1×10^8
Δu(cm/s)	...	3.2×10^6	
Perpendicular velocity $\sqrt{u_x^2 + u_y^2}$(cm/s)	...	2.7×10^6	1.5×10^7
Sound speed c_s (cm/s)	$9.8 \times 10^5 \frac{[ZT_{\rm ele}+1.67T_{\rm ion}]^{1/2}}{A^{1/2}}$	2.0×10^7	1.6×10^7
Mach number M	u/c_s	5.5	6.8
Electron plasma frequency (rad/s)	$5.6 \times 10^4 n_e^{1/2}$	7.9×10^{14}	3.1×10^{14}
Coulomb logarithm $\ln\Lambda$	$23.5 - \ln(n_e^{1/2}T_e^{-5/4}) - [10^{-5} + (\ln T_e - 2)^2/16]^{1/2}$	6.9	7.5
Electron thermal velocity v_{Te} (cm/s)	$4.2 \times 10^7 T_e^{1/2}$	9.5×10^8	8.3×10^8
Electron collision rate ν_e (1/s)	$2.9 \times 10^{-6} n_e \ln\Lambda T_e^{-3/2}$	3.5×10^{11}	8.5×10^{10}
Electron-ion collision rate ν_{ei} (1/s)	$3.2 \times 10^{-9} ZA^{-1} n_e \ln\Lambda T_e^{-3/2}$	2.1×10^8	5.1×10^7
Electron mean free path l_e (cm)	$v_{\rm Te}/\nu_e$	2.7×10^{-3}	9.8×10^{-3}
Electron gyro-frequency ω_{ce} (rad/s)	$1.7 \times 10^7 B$	5.6×10^{12}	7.8×10^{11}
Electron gyroradius r_e (cm)	$2.4 T_e^{1/2} B^{-1}$	1.6×10^{-4}	7.0×10^{-4}
Ion thermal velocity v_{Ti} (cm/s)	$9.8 \times 10^5 A^{-1/2} T_i^{1/2}$	9.2×10^6	2.9×10^6
Ion collision rate ν_i (1/s)	$4.8 \times 10^{-8} Z^3 n_e A^{-1/2} \ln\Lambda T_i^{-3/2}$	8.2×10^{10}	1.8×10^{14}
Ion mean free path l_i (cm)	$v_{\rm Ti}/\nu_i$	1.1×10^{-4}	1.6×10^{-8}
Ion gyro-frequency ω_{ci} (rad/s)	$9.6 \times 10^3 ZB/A$	1.7×10^9	2.4×10^8
Ion gyroradius r_i (cm)	$1.0 \times 10^2 A^{1/2} Z^{-1} T_i^{1/2} B^{-1}$	5.3×10^{-3}	2.1×10^{-2}
Plasma β	$\frac{2.4 \times 10^{-12} n_e(T_e + T_i/Z)}{B^2/(8\pi)}$	75	3.8×10^2
Kinetic energy/thermal energy	$\frac{\frac{1}{2}\frac{m_p n_e A}{Z}u^2}{2.4 \times 10^{-12} n_e(T_e + T_i/Z)}$	12	18
Reynolds number Rm	$uL\Big/\nu\left(\eta = 1.9 \times 10^{19}\frac{T_i^{5/2}}{A^{1/2}Z^3 n_e \ln\Lambda}\right)$	1.1×10^4	3.3×10^4
Magnetic Reynolds number Re	$uL\Big/\eta\left(\eta = 3.2 \times 10^5\frac{Z\ln\Lambda}{T_e^{3/2}}\right)$	1.6×10^4	1.0×10^4
Biermann number Bi	$\frac{euBL}{ck_B T_e}$	71	13
Hall number Ω_H	$\frac{4\pi e n_e uL}{Bc}$	1.3×10^3	1.4×10^3

electron temperature. The reason for this might be the usage of electron heat conduction in FLASH simulation, which mitigates the inaccuracy of energy apportion. The extra part of the ion thermal energy measured by the IAW spectrum can only come from part of the kinetic energy in the axial bulk motion of the flow, since multiple shocks already convert the kinetic energy of radial and toroidal bulk motion into thermal energy, and the magnetic energy is little compared to the thermal energy and the kinetic energy. For example, 10% of the bulk kinetic energy density at $t = 3$ ns and $z = 2.5$ mm corresponds to

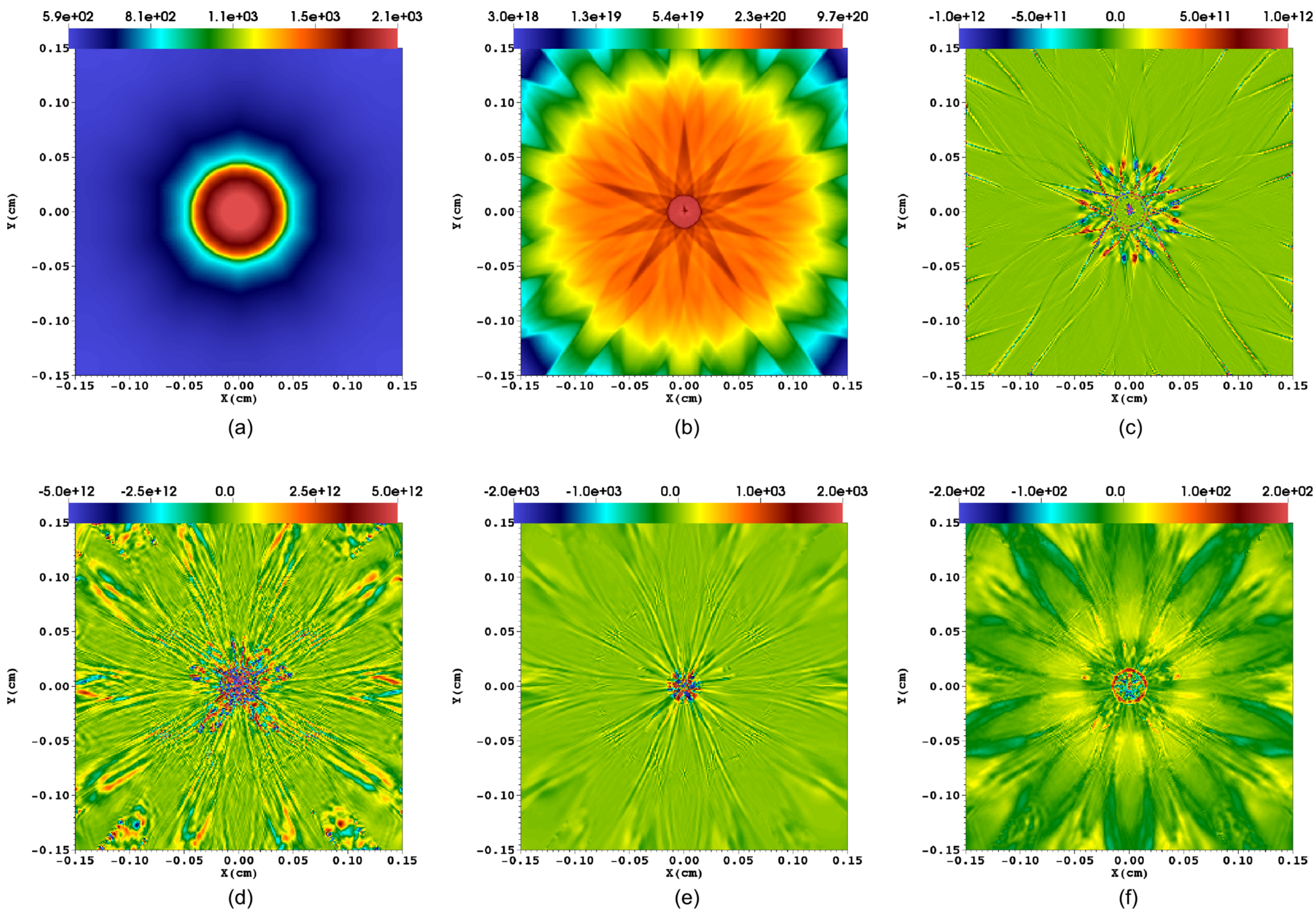

FIG. 7. Slice plot of several quantities at $z = 0.1$ cm for $t = 1.6$ ns. These figures demonstrate the generation and evolution of the axial dominant magnetic field with alternating polarity and 5-fold symmetry (a) Electron temperature (eV). The pattern is concentric circles. (b) Electron density (cm^{-3}). The "sunflower-like" pattern has 5-fold symmetry due to the laser pattern. The symmetry is slightly broken due to the finite number of cells in the simulation (c) z component of the Biermann battery term $\frac{c}{e}\nabla\times\frac{\nabla P_e}{n_e} = \frac{ck_B}{e}\nabla T_e\times\nabla n_e$ (kG/s), (d) z component of the advection term $\nabla\times(\boldsymbol{v}\times\mathbf{B})$ (kG/s), (e) z component of the magnetic field (kG), and (f) φ component of the magnetic field (kG).

$k_B T_i = 0.1\times\frac{m_i u^2}{2}\approx 2$ keV. It is likely that the turbulence is developed from the flow velocity difference between the plumes generated from different laser spots due the laser intensity difference between these spots. The plasma has a high Reynolds number, as shown in Table IV. The kinetic energy in turbulent motion does not have to be dissipated into heat to make the IAW spectrum broader, as long as a significant amount of turbulent kinetic energy is cascaded down to a scale below the resolution of Thomason scattering, i.e., $\sim$100 μm. We will study the turbulence effect in a future work.

B. Proton radiography

The proton images are smeared by a few factors (1) Spatial smearing: the finite size of the proton source, which is $\sim$45 μm for the fusion protons and $\sim$5 μm for the TNSA protons; (2) Temporal smearing: the pulse duration of the proton source, which is $\sim$150 ps for fusion protons and 1 ps for TNSA protons. The pulse duration Δt causes the smearing at the length scale $\Delta l\sim v\Delta t$, where v is the characteristic speed of the plasma. For fusion protons, $\Delta l_z\sim 160\,\mu$m, $\Delta l_{x,y}\sim 13\,\mu$m, using the velocities in Table IV. For TNSA protons with E = 10 MeV, $\Delta l_z\sim 1\,\mu$m, $\Delta l_{x,y}\sim 0.15\,\mu$m; (3) Spectrum smearing: the energy variation ΔE of the source proton. Derived from Eq. (16) in the study by Graziani *et al.*,[35] the variation of the deflection angle caused by ΔE is $\frac{\Delta E}{2E}$ times the deflection angle. If there is only spectrum smearing, assuming that the proton is shifted by 200 μm (which is typical) seen in the TCC frame, it is expected that the 10.2 MeV TNSA protons with $\frac{\Delta E}{2E}=\frac{3.79\mathrm{MeV}/2}{2\times 10.2\mathrm{MeV}}$ (ΔE is half of the effective temperature) resolve the magnetic field at $\sim$20 μm, DD protons with $\frac{\Delta E}{2E}=\frac{0.32\mathrm{MeV}}{2\times 3\mathrm{MeV}}$ resolve the magnetic field at $\sim$11 μm, and D^{3}He protons with $\frac{\Delta E}{2E}=\frac{0.67\mathrm{MeV}}{2\times 14.7\mathrm{MeV}}$ resolve the magnetic field at $\sim$5 μm. The energy gain or lost from the electric field is estimated to be less than 0.1 MeV, which is negligible compare to ΔE of the beam itself. Overall, our FLASH simulation is able to resolve a smaller spatial scale than the experiment.

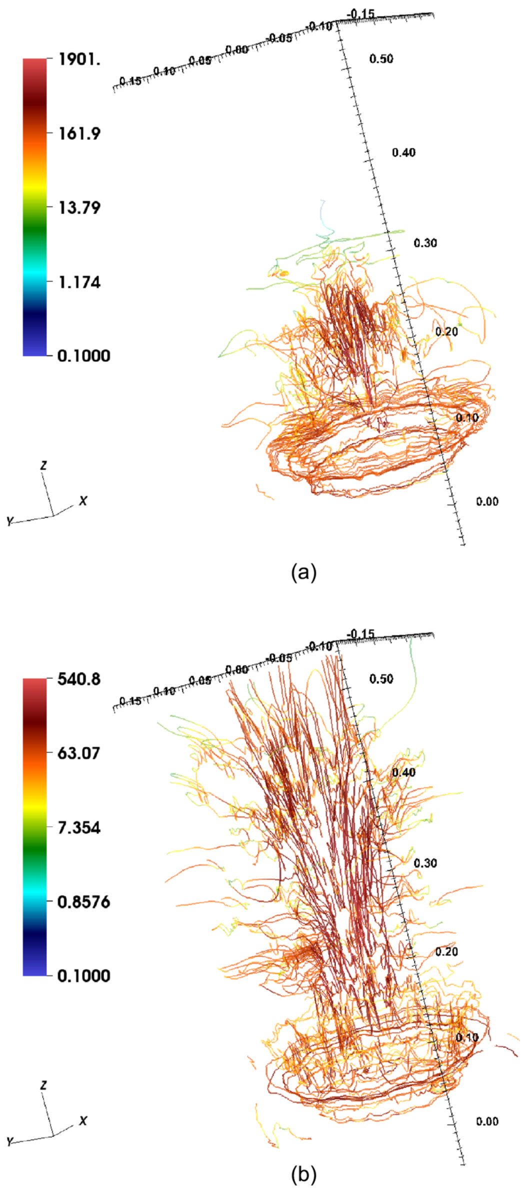

FIG. 8. Sample magnetic field lines (color scale unit: kG) for $d = 800$ cm, CH target. (a) at $t = 1.6$ ns (b) at $t = 3.6$ ns. The field far away from the target is mainly axial and the field close to the target is toroidal.

The simulation of images predicts the features observed in the experimental data. To the lowest order, the light and dark patterns correspond to the averaged MHD current ($\nabla \times \mathbf{B}$) projected along the light of sight.[35] The alternating axial field filaments result in several vertical dark and bright strips. The curved horizontal strip close to the surface of the target is produced by the large loop of the surface toroidal field. Figure 13 shows the comparison between the simulation synthetic and experimental D^3He proton images. Figure 14 shows the comparison between the simulation synthetic and experimental

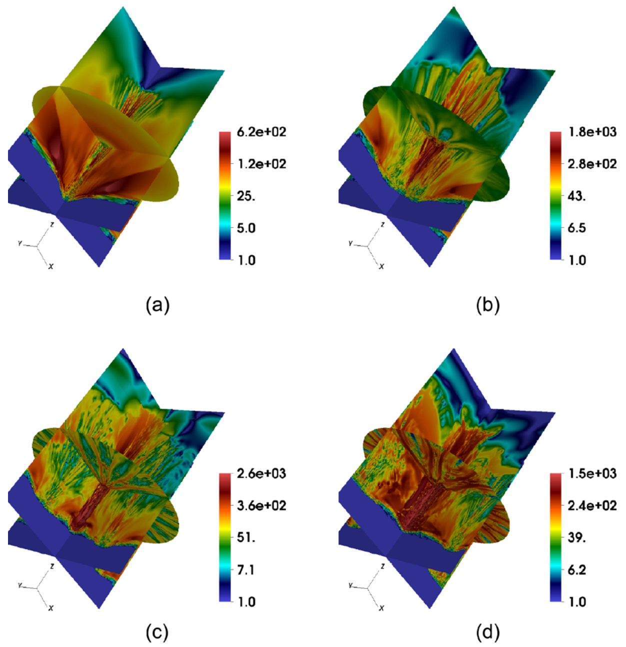

FIG. 9. Three slice plot for magnetic field amplitude (unit:kG) at $x = 0$, $y = 0$, and $z = 0.1$ cm for different laser ring radii d at $t = 1.6$ ns. The disk slice is at $z = 0.1$ cm with a diameter of 0.3 mm. (a) $d = 0$, (b) $d = 400\,\mu$m, (c) $d = 800\,\mu$m, and (d) $d = 1200\,\mu$m.

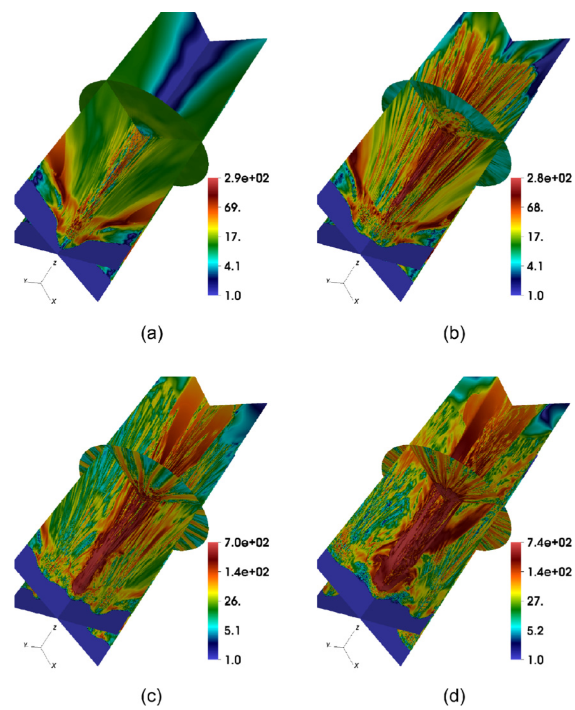

FIG. 10. Three slice plot for magnetic field amplitude (unit:kG) at $x = 0$, $y = 0$, and $z = 0.25$ cm for different laser ring radii d at $t = 3.6$ ns. The disk slice is at $z = 0.25$ cm with a diameter of 0.3 mm. (a) $d = 0$, (b) $d = 400\,\mu$m, (c) $d = 800\,\mu$m, and (d) $d = 1200\,\mu$m.

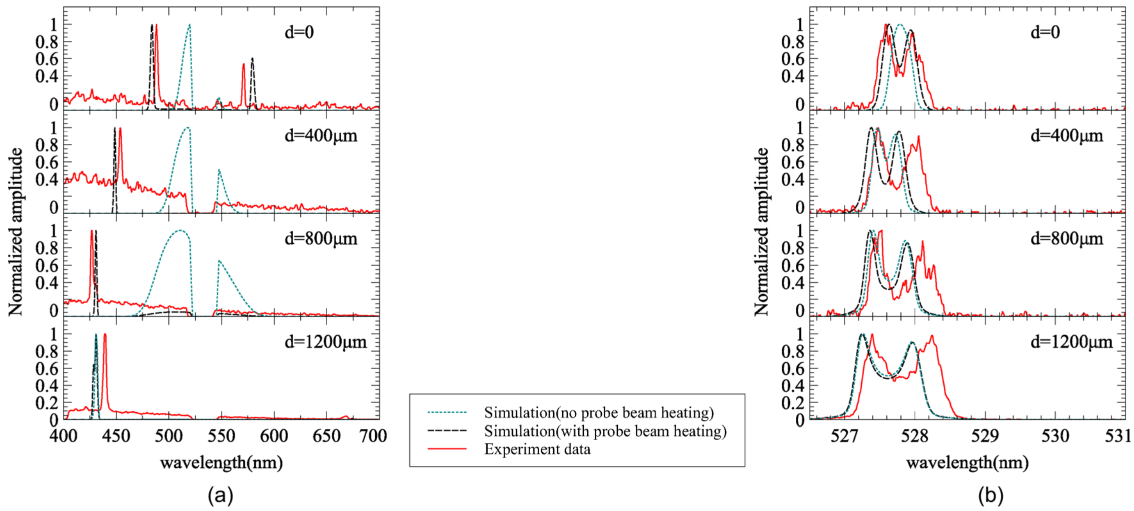

FIG. 11. Comparison between the synthetic optical Thomson-scattering spectra based on FLASH simulations and the experimental data. The red solid line is the experimental data, the blue dotted line is the synthetic spectrum without probe beam heating, and the black dashed line is the synthetic spectrum with probe beam heating. (a) EPW spectrum at 3.6 ns. (b) IAW spectrum at 3.9 ns.

10.2 MeV TNSA proton images. Figure 15 shows examples of the proton images for $d = 400\ \mu$m and $d = 1200\ \mu$m cases. Good qualitative agreement between the synthetic images and the ones from experiment on the general trend of large scale features suggests that the magnetic field structures we predict using FLASH simulation are consistent with the structures in the experiments.

The Nernst effect can affect the evolution of the magnetic field.[36,37] This might be the reason why there are some disagreements in small scale structures and sizes between the experimental data and the synthetic images. In Table IV, the product of the electron gyro-frequency ω_{ce} and electron collision time $\tau_e (= 1/\nu_e)$ is $\omega_{ce}\tau_e \sim 15$ at $r = 0$ and $\omega_{ce}\tau_e \sim 9$ at $r = 1$ mm. The value $\omega_{ce}\tau_e > 1$ indicates that the Nernst effect is important for our experiments. The MHD model with the Nernst term will be implemented in FLASH in the future. We will make detailed qualitative comparison in a future study with the Nernst term included.

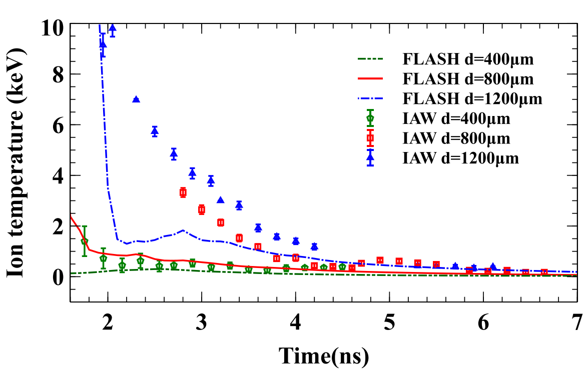

FIG. 12. The data for ion temperature from fitting the IAW spectrum and the $(200\ \mu\text{m})^3$ averaged value in FLASH simulations, both at TCC.

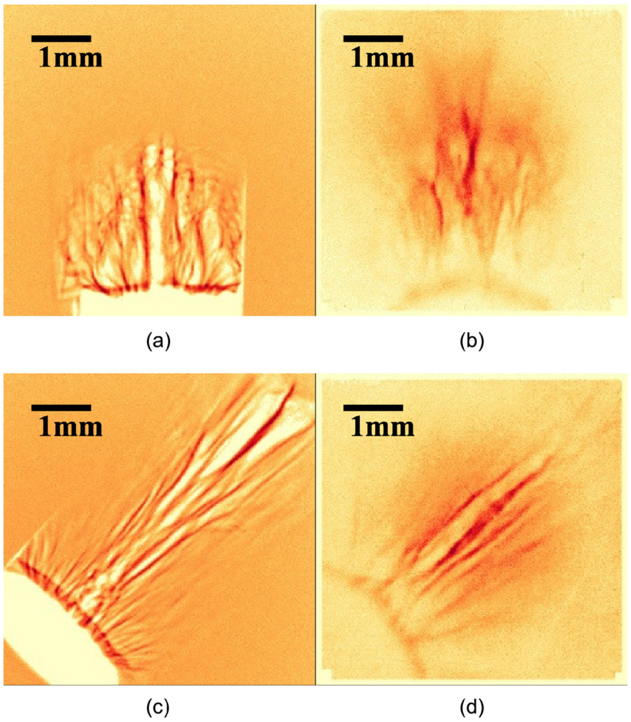

FIG. 13. Comparison of the synthetic proton image with data recorded on CR39 for 14.7 MeV protons. The color scales are the same for all images. The ring radius is $d = 800\ \mu$m. The target is CH without the dopant. (a) The synthetic image at $t = 1.6$ ns, and the corresponding three-slice plot of the field is in Fig. 9(c). (b) The experimental image at $t = 1.6$ ns, (c) synthetic image at $t = 3.6$ ns, and the corresponding three-slice plot of the field is in Fig. 10(c). (d) The experimental image at $t = 3.6$ ns. The CR39 image plate is 10 cm $\times$ 10 cm. On the plot, magnification is taken into account, and the scale listed is in the plasma frame. In (a) and (b), upward is the $+z$ direction. In (c) and (d), upright is the $+z$ direction. The void region in below in (a) and (b), and bottom left corner in (c) and (d) is the target, which block the protons.

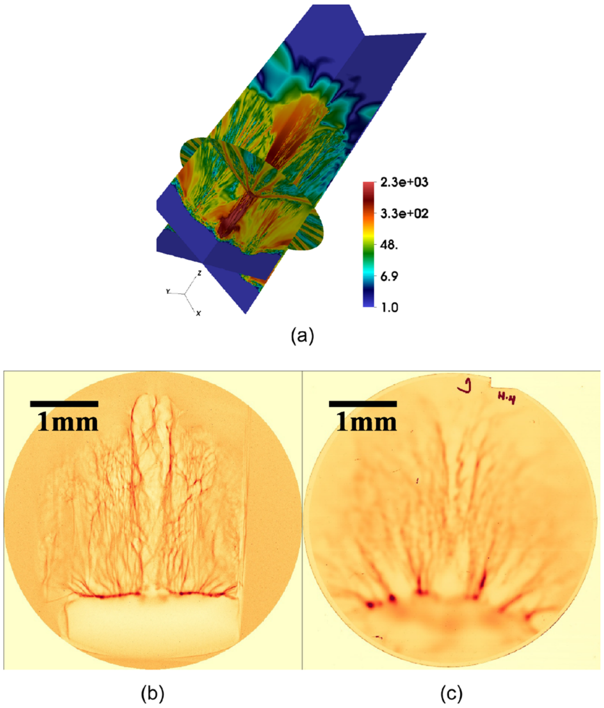

FIG. 14. Comparison of the synthetic proton image with data recorded on the radiochromic film for 10.2MeV protons. The color scales are the same for two images. The ring radius is $d = 800\ \mu m$. The target is CH without dopant. (a) three-slice plot at $x = 0$, $y = 0$, $z = 0.1$ cm, magnetic field strength (kG) plot at $t = 1.9$ ns, (b) synthetic image at $t = 1.9$ ns, and (c) experimental image at $t = 1.9$ ns from H4 pack. The image plate is a disk of 10 cm. The scale and orientation are the same as in Figs. 13(a) and 13(b).

V. CONCLUSIONS AND DISCUSSIONS

The FLASH simulation results were validated against a subset of experimental data from the OMEGA experiments. The creation of the jets and strong magnetic fields using the ring laser pattern is explained. 3D simulations reproduce some features in previous 2D cylindrical results.[14,15] However, many new features emerge in 3D, e.g., the "sun flower" density pattern and the alternating para-axial magnetic field bundles. Some questions still remain, e.g., the under-prediction in the line width of the IAW spectrum in Fig. 11. An accurate modeling for the magnetic fields requires implementation of the Nernst effect in the FLASH code. Simulations using higher resolutions are also desired. The XRFC modeling will be discussed in a future study.

The geometry of magnetic fields in our jets may be different from the generally believed models in many astrophysical context, e.g., the magnetic field of the jet along the axis of an accreting black hole,[38] where the toroidal field supposedly dominates. However, much can still be learned about the magnetic effect on jet collimation, stability, and structure in the laboratory. The characteristics of the magnetized jet can be well controlled by tuning the ring radius and increasing number of beams. By varying the hollow ring radius, laser, and target properties, we can achieve a large dynamic range for the jet parameters, thus creating a highly versatile laboratory platform for laser-based astrophysics. By using the jets we created, shocks and shear flows can be studied with jet-jet collisions.

The hollow ring laser platform is also ideally suited to scale up to NIF with 192 beams and more energy per beam, creating centimeter-sized magnetized jets. The jets produced with the

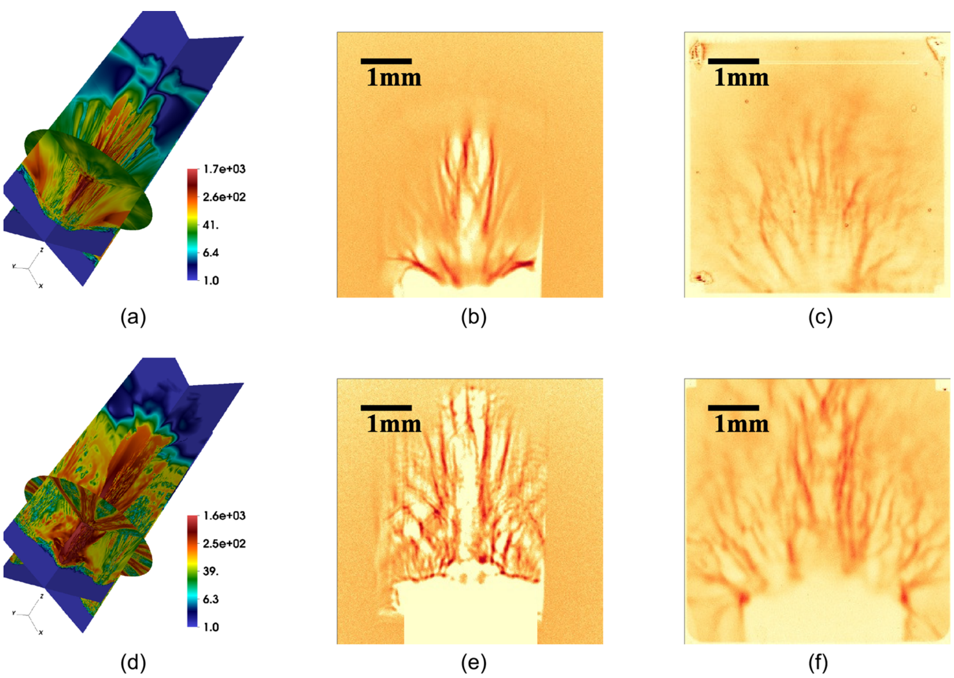

FIG. 15. (a) Three-slice plot at $x = 0$, $y = 0$, and $z = 0.1$ cm and the magnetic field strength (kG) plot at $t = 1.8$ ns for $d = 400\ \mu m$. (b) The synthetic 3MeV proton image at $t = 1.8$ ns for $d = 400\ \mu m$. (c) The experimental 3MeV proton image at $t = 1.9$ ns for $d = 400\ \mu m$. (c) Three-slice plot at $x = 0$, $y = 0$, and $z = 0.1$ cm and magnetic field strength (kG) plot at $t = 2.3$ ns for $d = 120\ \mu m$. (d) The synthetic 14.7MeV proton image at $t = 2.3$ ns for $d = 1200\ \mu m$. (e) The experimental 14.7MeV proton image at $t = 2.3$ ns for $d = 1200\ \mu m$. The scale and orientation of the image are the same as in Figs. 13(a) and 13(b). The color scales are the same for all images.

NIF platform will have several distinctive properties from OMEGA experiments but are of key importance for astrophysical jet modeling. The higher temperature, density, flow velocity, and magnetic field will lead to large dimensionless parameters. A turbulence regime is possible. The longer pulse on NIF can sustain the jet for longer time, so that the radiative cooling for doped targets becomes significant and useful to make the aspect ratio larger. The aspect ratio can become large enough ($\gg 10$) that the stability study can become more relevant to astrophysics. The physical parameters of the jet can be tuned in such ways that various collisionless and collisional regimes of the plasma can be accessed. The dimensionless parameters for astrophysical jets may be better realized in the large scale jets of NIF. Magnetic field geometry may be tuned by increasing the number of beams.

ACKNOWLEDGMENTS

This research was supported by DOE Grant DE-NA0002721. The research and materials incorporated in this work were partially developed at the National Laser Users' Facility at the University of Rochester's Laboratory for Laser Energetics (LLE), with the financial support from the U.S. Department of Energy (DOE) under Cooperative Agreement DE-NA0001944. This work used the Extreme Science and Engineering Discovery Environment (XSEDE[39]) which was supported by the National Science Foundation (NSF) Grant No. ACI-1548562. This research used resources of the National Energy Research Scientific Computing Center, a DOE Office of Science User Facility supported by the Office of Science of the U.S. Department of Energy under Contract No. DE-AC02-05CH11231. Additional simulations were performed at the Argonne Leadership Computing Facility and with Los Alamos National Laboratory institutional computing. Y.L. and E.L. acknowledge partial support by LANL-LDRD during the writing of this paper. We also acknowledge the valuable discussions with Hui Li.

REFERENCES

[1] S. Hirose, Y. Uchida, K. Shibata, and R. Matsumoto, Publ. Astron. Soc. Jpn. **49**, 193 (1997).
[2] A. Ferrari, Annu. Rev. Astron. Astrophys. **36**, 539 (1998).
[3] R. Sari, T. Piran, and J. P. Halpern, Astrophys. J. **519**, L17 (1999).
[4] P. Tzeferacos, A. Rigby, A. Bott, A. R. Bell, R. Bingham, A. Casner, F. Cattaneo, E. M. Churazov, J. Emig, N. Flocke, F. Fiuza, C. B. Forest, J. Foster, C. Graziani, J. Katz, M. Koenig, C.-K. Li, J. Meinecke, R. Petrasso, H.-S. Park, B. A. Remington, J. S. Ross, D. Ryu, D. Ryutov, K. Weide, T. G. White, B. Reville, F. Miniati, A. A. Schekochihin, D. H. Froula, G. Gregori, and D. Q. Lamb, Phys. Plasmas **24**, 041404 (2017).
[5] P. Tzeferacos, A. Rigby, A. F. A. Bott, A. R. Bell, R. Bingham, A. Casner, F. Cattaneo, E. M. Churazov, J. Emig, F. Fiuza, C. B. Forest, J. Foster, C. Graziani, J. Katz, M. Koenig, C.-K. Li, J. Meinecke, R. Petrasso, H.-S. Park, B. A. Remington, J. S. Ross, D. Ryu, D. Ryutov, T. G. White, B. Reville, F. Miniati, A. A. Schekochihin, D. Q. Lamb, D. H. Froula, and G. Gregori, Nat. Commun. **9**, 591 (2018).
[6] B. A. Remington, Plasma Phys. Controlled Fusion **47**, A191 (2005).
[7] J. M. Foster, B. H. Wilde, P. A. Rosen, R. J. R. Williams, B. E. Blue, R. F. Coker, R. P. Drake, A. Frank, P. A. Keiter, A. M. Khokhlov, J. P. Knauer, and T. S. Perry, Astrophys. J. **634**, L77 (2005).
[8] A. Ciardi, S. V. Lebedev, A. Frank, E. G. Blackman, J. P. Chittenden, C. J. Jennings, D. J. Ampleford, S. N. Bland, S. C. Bott, J. Rapley, G. N. Hall, F. A. Suzuki-Vidal, A. Marocchino, T. Lery, and C. Stehle, Phys. Plasmas **14**, 056501 (2007).
[9] A. Ciardi, S. V. Lebedev, A. Frank, F. Suzuki-Vidal, G. N. Hall, S. N. Bland, A. Harvey-Thompson, E. G. Blackman, and M. Camenzind, Astrophys. J. **691**, L147 (2009).
[10] S. V. Lebedev, D. Ampleford, A. Ciardi, S. N. Bland, J. P. Chittenden, M. G. Haines, A. Frank, E. G. Blackman, and A. Cunningham, Astrophys. J. **616**, 988 (2004).
[11] S. V. Lebedev, A. Ciardi, D. J. Ampleford, S. N. Bland, S. C. Bott, J. P. Chittenden, G. N. Hall, J. Rapley, C. Jennings, M. Sherlock, A. Frank, and E. G. Blackman, Plasma Phys. Controlled Fusion **47**, B465 (2005).
[12] S. V. Lebedev, J. P. Chittenden, F. N. Beg, S. N. Bland, A. Ciardi, D. Ampleford, S. Hughes, M. G. Haines, A. Frank, E. G. Blackman, and T. Gardiner, Astrophys. J. **564**, 113 (2002).
[13] B. A. Remington, R. P. Drake, and D. D. Ryutov, Rev. Mod. Phys. **78**, 755 (2006).
[14] W. Fu, E. P. Liang, M. Fatenejad, D. Q. Lamb, M. Grosskopf, H.-S. Park, B. Remington, and A. Spitkovsky, High Energy Density Phys. **9**, 336 (2013).
[15] W. Fu, E. P. Liang, P. Tzeferacos, and D. Q. Lamb, High Energy Density Phys. **17**, 42 (2015).
[16] L. Biermann, Z. Naturforsch., A **5**, 65 (1950); available at http://adsabs.harvard.edu/abs/1950ZNatA...5...65.
[17] T. Boehly, D. Brown, R. Craxton, R. Keck, J. Knauer, J. Kelly, T. Kessler, S. Kumpan, S. Loucks, S. Letzring, F. Marshall, R. McCrory, S. Morse, W. Seka, J. Soures, and C. Verdon, Opt. Commun. **133**, 495 (1997).
[18] L. Gao *et al.*, "Mega-gauss plasma jet creation using a ring of laser beams" (unpublished).
[19] B. Fryxell, K. Olson, P. Ricker, F. X. Timmes, M. Zingale, D. Q. Lamb, P. MacNeice, R. Rosner, J. W. Truran, and H. Tufo, Astrophys. J. Suppl. Ser. **131**, 273 (2000).
[20] See https://flash.uchicago.edu/ for FLASH4.
[21] A. Dubey, K. Antypas, M. K. Ganapathy, L. B. Reid, K. Riley, D. Sheeler, A. Siegel, and K. Weide, Parallel Comput. **35**, 512 (2009).
[22] C. Graziani, P. Tzeferacos, D. Lee, D. Q. Lamb, K. Weide, M. Fatenejad, and J. Miller, Astrophys. J. **802**, 43 (2015).
[23] See http://www.prism-cs.com for PROPACEOS.
[24] S. I. Braginskii, Rev. Plasma Phys. **1**, 205 (1965); available at http://adsabs.harvard.edu/abs/1965RvPP....1..205B.
[25] D. H. Froula, J. S. Ross, L. Divol, and S. H. Glenzer, Rev. Sci. Instrum. **77**, 10E522 (2006).
[26] D. Froula, P. Davis, L. Divol, J. Ross, N. Meezan, D. Price, S. Glenzer, and C. Rousseaux, Phys. Rev. Lett. **95**, 195005–195009 (2005).
[27] J. Sheffield, D. Froula, S. H. Glenzer, and J. N. C. Luhmann, *Plasma Scattering of Electromagnetic Radiation: Theory and Measurement Techniques* (Academic Press, 2010).
[28] R. K. Follett, J. A. Delettrez, D. H. Edgell, R. J. Henchen, J. Katz, J. F. Myatt, and D. H. Froula, Rev. Sci. Instrum. **87**, 11E401 (2016).
[29] C. K. Li, F. H. Séguin, J. A. Frenje, J. R. Rygg, R. D. Petrasso, R. P. J. Town, P. A. Amendt, S. P. Hatchett, O. L. Landen, A. J. Mackinnon, P. K. Patel, V. A. Smalyuk, T. C. Sangster, and J. P. Knauer, Phys. Rev. Lett. **97**, 135003 (2006).
[30] M. J.-E. Manuel, A. B. Zylstra, H. G. Rinderknecht, D. T. Casey, M. J. Rosenberg, N. Sinenian, C. K. Li, J. A. Frenje, F. H. Séguin, and R. D. Petrasso, Rev. Sci. Instrum. **83**, 063506 (2012).
[31] A. B. Zylstra, C. K. Li, H. G. Rinderknecht, F. H. Séguin, R. D. Petrasso, C. Stoeckl, D. D. Meyerhofer, P. Nilson, T. C. Sangster, S. L. Pape, A. Mackinnon, and P. Patel, Rev. Sci. Instrum. **83**, 013511 (2012).
[32] K. Flippo, T. Bartal, F. Beg, S. Chawla, J. Cobble, S. Gaillard, D. Hey, A. MacKinnon, A. MacPhee, P. Nilson, D. Offermann, S. L. Pape, and M. J. Schmitt, J. Phys.: Conf. Ser. **244**, 022033 (2010).
[33] See https://physics.nist.gov/PhysRefData/Star/Text/PSTAR.html for The PSTAR Table.
[34] M. Gittings, R. Weaver, M. Clover, T. Betlach, N. Byrne, R. Coker, E. Dendy, R. Hueckstaedt, K. New, W. R. Oakes, D. Ranta, and R. Stefan, Comput. Sci. Discovery **1**, 015005 (2008).

[35]C. Graziani, P. Tzeferacos, D. Q. Lamb, and C. Li, Rev. Sci. Instrum. **88**, 123507 (2017).
[36]L. Gao, P. Nilson, I. Igumenshchev, M. Haines, D. Froula, R. Betti, and D. Meyerhofer, Phys. Rev. Lett. **114**, 215003 (2015).
[37]L. Lancia, B. Albertazzi, C. Boniface, A. Grisollet, R. Riquier, F. Chaland, K.-C. L. Thanh, P. Mellor, P. Antici, S. Buffechoux, S. Chen, D. Doria, M. Nakatsutsumi, C. Peth, M. Swantusch, M. Stardubtsev, L. Palumbo, M. Borghesi, O. Willi, H. Pépin, and J. Fuchs, Phys. Rev. Lett. **113**, 235001 (2014).
[38]K. Beckwith, J. F. Hawley, and J. H. Krolik, Astrophys. J. **678**, 1180 (2008).
[39]J. Towns, T. Cockerill, M. Dahan, I. Foster, K. Gaither, A. Grimshaw, V. Hazlewood, S. Lathrop, D. Lifka, G. D. Peterson, R. Roskies, J. R. Scott, and N. Wilkens-Diehr, Comput. Sci. Eng. **16**, 62 (2014).